



Evanescent waves in hybrid poroelastic metamaterials with interface effects

Shu-Yan Zhang ^a, Jia-Chen Luo ^b, Yan-Feng Wang ^{c,*}, Vincent Laude ^d, Yue-Sheng Wang ^{a,c}

^a Institute of Engineering Mechanics, Beijing Jiaotong University, 100044 Beijing, China

^b State Key Laboratory of Structural Analysis for Industrial Equipment, Department of Engineering Mechanics, Dalian University of Technology, Dalian 116023, China

^c Department of Mechanics, School of Mechanical Engineering, Tianjin University, 300350 Tianjin, China

^d Institut FEMTO-ST, CNRS, Univ. Bourgogne Franche-Comté, 25030 Besançon, France



ARTICLE INFO

Keywords:

Hybrid poroelastic metamaterials
Interface effects
Single-phased and poroelastic system
Complex band structures

ABSTRACT

The propagation of evanescent waves in hybrid poroelastic metamaterials is investigated by considering interface effects. Hybrid metamaterials consist of a single-phased (acoustic or elastic) medium and a poroelastic medium. To establish the finite element model of elastic/poroelastic and fluid/poroelastic interfaces, weak integral forms of wave equations for elastic, fluid, and poroelastic media and boundary conditions at the interfaces between different media are first given. Next, the expressions for displacement and pressure in the frame of Bloch's theorem are substituted into the dynamical equations to obtain general forms suitable for periodic metamaterials, from which the complex band structure and the frequency response of hybrid metamaterials are calculated. The influence of geometrical and material parameters, as well as the viscosity of the pore fluid on the propagation of elastic waves are discussed. The results and discussions show that flat bands and narrow locally resonant band gaps appear for elastic/poroelastic metamaterials. A quasi-resonance Bragg band gap is formed in the case of an elastic inclusion in a poroelastic matrix. Furthermore, a transition from an avoided crossing to a wave-number band gap is obtained by adjusting the geometrical and material parameters of the elastic inclusion. For the case of fluid inclusion in a poroelastic matrix with the open-pore interface, a cut-off frequency for the fast longitudinal wave is observed. However, only an avoided crossing is produced for the sealed-pore interface. For both cases, the phase velocity of the shear vertical (SV) wave decreases faster than that of the slow longitudinal wave as the radius of the inclusion increases. When the viscosity of the pore fluid is considered for elastic inclusion in a poroelastic matrix, the transmission dip at the 'quasi-resonance Bragg' band gap disappears. However, the transmission dip in the locally resonant band gap of the SV wave becomes slightly shallower and smoother than in the inviscid case. This study is relevant to practical applications of hybrid single-phased and poroelastic metamaterials, e.g., for coastal engineering and civil engineering.

1. Introduction

Phononic crystals [1] (PCs) and metamaterials [2] are artificial composite materials. Their remarkable feature is the existence of band gaps, within which the propagation of acoustic or elastic waves is prohibited. Phononic crystals and metamaterials are widely used to design noise barriers [3] and vibration isolators [4], among other applications. Bragg scattering [1] and local resonance [5] are two basic mechanisms for band gap generation. It is worth underlining that band gaps are not only strongly affected by geometric parameters and material properties, but also by interface conditions. For example, solid/solid smooth-contact interfaces [6], fluid/fluid interfaces [7], solid/fluid interfaces [8], and imperfect interfaces [9] all deeply influence wave propagation. Until now, most studies on metamaterials

have focused on single-phased media, but poroelastic media are often involved in terrestrial applications.

Poroelastic media are generally considered to be composed of a solid skeleton and a fluid contained inside the pores. They have far and wide applications in geophysics exploration [10], coastal engineering [11], seismology engineering [12], and other fields [13]. Biot [14] first developed a theory of the poroelastic medium and predicted that two longitudinal waves (fast and slow) and two shear waves (SV wave) co-exist. Due to the presence of the slow-longitudinal wave, the mathematical description of the interface between poroelastic and other media is more complicated than the interface between different single-phased media. Deresiewicz and Skalak [15] derived interface conditions between two poroelastic media. The equations of the impermeable interface between elastic and poroelastic media and the

* Corresponding author.

E-mail addresses: wangyanfeng@tju.edu.cn (Y.-F. Wang), yswang@tju.edu.cn (Y.-S. Wang).

open-pore interface between fluid and poroelastic media were also given by the same authors. However, the presence of the fluid in the solid skeleton may weaken the contact at the interface. Hence, it can cause the elastic and poroelastic interfaces to be loosely bonded [16]. For the fluid/poroelastic interface, two other boundary conditions have been proposed to describe hydraulic contacts: sealed pores [17] and imperfect pores involving the hydraulic permeability of the interface [18]. Since then, many researchers have studied wave propagation in poroelastic media using those interface conditions. They can be roughly divided into the following three categories.

First, the interface between two different poroelastic media has received much attention. Various boundary conditions have been proposed to describe interface contacts: open-pore, partial-open pore, and sealed-pore interfaces. For the open-pore interface, many researchers have calculated reflection and transmission coefficients at the interface between two half-spaces: two porous media filled with an immiscible fluid [19], two dissimilar poroelastic solids saturated with two immiscible viscous fluids [20], the coupled porous sediment, and the double-porosity substrate [21]. For the sealed-pore interface, Rasolofosaon [22] first described the importance of generating the slow compressional wave in porous media. Smeulders [23] analyzed the reflection coefficient and the pressure distribution of slow-compressional waves and guessed that there are additional damping mechanisms that are not incorporated in the theory. Dai et al. [24] introduced a double porosity solid and discussed its influence on reflection and transmission. The last interface type is the partial open-pore interface. Sharma and Saini [25] analyzed the effect of pore alignment on amplitude ratios and energy ratios. Next, Sharma [26] regarded the partial connection of surface pores at the interface as tangential slipping and discussed wave propagation. Vashishth and Khurana [27] considered multilayered anisotropic poroelastic media and calculated reflection and transmission coefficients.

Second, the interface between elastic and poroelastic media is also of great interest. The impermeability interface is widely considered in applications [28]. Some researchers are concerned with the impermeable interface; Dai et al. [29] developed a theoretical analysis of elastic wave reflection and transmission at the interface between elastic and double porosity half-spaces. Wang et al. [30] investigated the energy dissipation of the porous sediment at the porous/solid interface. Sharma et al. [31,32] considered the effect of solid viscoelasticity and fluid viscosity on plane harmonic waves' reflection and refraction. Peng et al. [33] gave wavefield snapshots of plane-wave propagation through the elastic/poroelastic system. Considering a permeable interface, Goyal and Tomar [34] dealt with the reflection and refraction of a plane longitudinal wave. Yang [35] numerically investigated the influence of incident angle and frequency on the transmission coefficient. Barak et al. [36] further discussed plane wave propagation at an interface between double-porosity solid with underlying uniform elastic solid. For a loosely bonded interface, Vashishth et al. [37] solved the problem of reflection and transmission of a plane incident wave, and found there is the dissipation of energy except for normal and grazing angles of incidence. Baljeet and Surjeet [38] introduced a viscous liquid into a porous solid to observe the relationship between reflection and refraction amplitude ratios for the incidence of P and SV waves.

Third, acoustic/poroelastic interface contacts were also examined. For the open-pore interface, Denneman et al. [39] derived closed-form expressions for reflection and transmission coefficients between acoustic and porous half-spaces. Lyu et al. [21] calculated the reflection and transmission of plane waves at the interface between the ocean and the ocean floor. Bouzidi and Schmitt [40] experimentally measured the acoustic reflection from a fluid/poroelastic interface as a function of the angle of incidence. For the sealed-pore interface, Denneman et al. [41] studied wave scattering at the interface of fluid/air-filled porous layers. Dai and Kuang [42] analyzed the reflection and transmission of elastic waves at the interface of a fluid and a double porosity

solid. Wu et al. [43] calculated reflection and transmission for a three-layer system consisting of a fluid-saturated porous layer sandwiched between a fluid half-space and a fluid substrate interface. For the partial open-pore interface, Chiavassa and Lombard [44] proposed an accurate numerical model to simulate wave propagation in fluid/poroelastic media. Mesgouez et al. [45] investigated transient wave propagation in a 2D acoustic/poroelastic system using semi-analytical and numerical methods.

Wave propagation in periodically arranged poroelastic media was not considered in the works cited above. In recent years, however, the propagation of elastic waves in porous metamaterials has been attracting increasing attention. Maglicano et al. [46] used an equivalent fluid model to describe a porous medium with a periodic arrangement of rigid inclusions; only one longitudinal wave is included in their model, however. Xiong et al. [47] proved that the periodic insertion of a rigid resonant inclusion into a porous matrix can enhance the attenuation of sound waves at low frequencies. Lewinska et al. [48] designed a porous microstructure combining a traditional poroelastic material with locally resonant units embedded inside the pores to strengthen the low-frequency attenuation of elastic waves. Though these researchers used foam as the porous medium, Biot's theory is not mentioned. Based on Biot's theory, Wang et al. [49,50] first studied wave propagation inside one-dimensional and two-dimensional fluid-saturated porous metamaterials with the open-pore interface, relying on finite element analysis of porous media. Zhang et al. [51] analyzed wave propagation in one-dimensional fluid-saturated porous metamaterials with the partial-open pore interface and enhanced the theoretical analysis of porous media. Fama et al. [52] theoretically described an incompressible fluid through the channels of a porous structure and analyzed the erosive/deposition effects of the fluid in a solid matrix. Rohan and Cimrman [53] explored porous scaffolds and the advection phenomenon of the disturbance caused by the wave superimposed on the fluid flow. Pu et al. [54] discussed the propagation of Rayleigh waves in seismic metamaterials consisting of mass-spring resonators periodically arranged on the surface of a porous half-space.

Although the studies above explicitly considered periodically saturated media, the interface between single-phased and poroelastic media was not discussed. As is well-known, acoustic [7], elastic [6], and poroelastic media [14] respectively support one (a longitudinal), three (a longitudinal and two shears), and four waves (two longitudinal and two shear) waves. Hence, in contrast to the interface between two poroelastic media, the propagation of a mechanical wave may change drastically at the interface between a single-phased medium and a poroelastic medium [29,30].

The purpose of this work is to study evanescent wave propagation in hybrid elastic/poroelastic and fluid/poroelastic periodic metamaterials. In this case, the complex band structure, rather than the real band structure, should be employed for analysis. Generally, the complex band structure can be computed following two different approaches: either the eigenfunction expansion method or the discrete method.

Based upon Bloch's theorem and series expansion theory, the eigenfunction expansion method expands the physical quantities appearing in the non-uniform wave equation into the series form. A generalized eigenvalue equation is formed by approximately considering finite expansion terms, such as the extended plane wave expansion (EPWE) method [55,56]. This method, however, generally cannot solve problems with complex interfaces [57]. Alternatively, it is possible to expand all scattered fields into cylindrical or spherical wave functions, taking advantage of symmetry, and then establish characteristic equations according to interface conditions and Bloch's theorem, resulting in methods such as multiple scattering theory [58] or Dirichlet to Neumann method [59]. Systems with complex interfaces can thus be handled, but only in the case of spherical or cylindrical scatterers.

In the case of the discrete method, the whole system is discretized, and the eigenvalue problem for the continuous system is transformed into a corresponding discrete problem suitable for numerical solving,

such as the finite element method (FEM) [60]. In the FEM framework, there are furthermore two different numerical approaches. One is to consider Bloch periodic boundary conditions around the unit cell. The complex band structure is then obtained by carefully transforming the global mass and stiffness matrices, resulting in the semi-analytical finite element method (SAFEM) [61] or the extended Bloch mode synthesis method (EBMSM) [62]. An alternative way is considering a Bloch operator transformation of the governing equation by substituting the Bloch wave solution into the governing equation, which is referred to as the Bloch operator finite element method (BOFEM) [63].

In the present work, the poroelastic medium acts as either the matrix or inclusions. The paper is organized as follows. In Section 2, wave equations are recalled for elastic, acoustic, and poroelastic domains and the corresponding weak integral forms are deduced. In Section 3, interface conditions between fluid/poroelastic, elastic/poroelastic, and poroelastic/poroelastic systems are given. The coupling boundary integrals at the resulting interfaces are specifically obtained. In Section 4, the unit cell and the partial differential equations are described. The simplification of interface conditions based on the weak integral formulation is extended to the case of periodic media. Section 5 presents complex band structures, modal distributions, and frequency responses for the poroelastic medium considered either as a matrix or inclusion, for both inviscid and viscous pore fluid. Meanwhile, the influence on wave propagation of geometric and material parameters of the inclusion, and the viscosity of the pore fluid, is also discussed. The main conclusions are drawn in Section 6.

2. Wave equations and weak integral forms

In this section, we turn our attention to the propagation of elastic waves in doubly-periodic media. For a given frequency, the wavelengths of acoustic, elastic, and porous media are different. Thus, we first give governing equations and derive the weak variational formulations for the three types of media. Boundary integrals between the three types of domains are then given.

2.1. Elastic wave equation and weak integral form

For vanishing body forces, the wave equation for an elastic medium can be written in the frequency domain as

$$\nabla \cdot \sigma^e + \rho^e \omega^2 \mathbf{u}^e = 0, \quad (1)$$

where $\sigma^e = \mathbf{C}(\mathbf{r}) : \nabla \mathbf{u}^e(\mathbf{r})$ and \mathbf{u}^e are stress and displacement vectors of the elastic solid; $\nabla = \left(\frac{\partial}{\partial x}, \frac{\partial}{\partial y}, \frac{\partial}{\partial z} \right)$ is the divergence operator; $\mathbf{C}(\mathbf{r})$ is the elastic tensor; $\mathbf{r} = (x, y, z)$ is the position vector; ρ^e is the mass density; and ω denotes the angular frequency.

Consider $\delta \mathbf{u}^e$ a test function of the displacement vector. According to the divergence or Gauss' theorem, the weak integral form of the previous equation for an elastic domain Ω_e can be expressed as

$$\int_{\Omega_e} \sigma^e : \epsilon^e (\delta \mathbf{u}^e) d\Omega_e - \int_{\Omega_e} \rho \omega^2 \mathbf{u}^e \cdot \delta \mathbf{u}^e d\Omega_e - \int_{S_e} \mathbf{n}^e \cdot \sigma^e \cdot \delta \mathbf{u}^e dS_e = 0. \quad (2)$$

where ϵ^e is the strain vector; S_e stands for the boundary; and \mathbf{n}^e is the external normal unit vector along S_e . The boundary integral in the last term is denoted I_e .

2.2. Acoustic wave equation and weak integral form

The governing equation for acoustic wave propagation in a homogeneous inviscid fluid is:

$$\nabla \cdot \left(\frac{1}{\omega^2 \rho^a} \nabla p^a \right) + \frac{1}{K^a} p^a = 0, \quad (3)$$

where ρ^a is the mass density of the fluid; p^a is the pressure; and $K^a = \rho^a c_a^2$ denotes the bulk modulus of the fluid with c_a the sound velocity in the fluid.

Consider δp^a a test function of the fluid pressure p^a . The weak integral form for the harmonic acoustic wave reads

$$\begin{aligned} & \int_{\Omega_a} \frac{1}{\omega^2 \rho^a} (\nabla p^a) \cdot \nabla (\delta p^a) d\Omega_a - \int_{\Omega_a} \frac{1}{K^a} p^a \delta p^a d\Omega_a \\ & - \int_{S_a} \frac{1}{\omega^2 \rho^a} \mathbf{n}^a \cdot (\nabla p^a) \cdot (\delta p^a) dS_a = 0, \end{aligned} \quad (4)$$

where Ω_a and S_a refer to the fluid domain and its boundary, respectively; and \mathbf{n}^a is the external normal unit vector along the boundary S_a . The boundary integral for pressure is denoted I_a .

2.3. Wave equations and weak integral forms for the poroelastic medium

Based on Biot's theory, the equations of motion of the isotropic poroelastic medium can be described by the macroscopic displacement vector (\mathbf{u}^s) of the solid phase and the pressure (p) of the fluid phase; see Appendix A. Combining the constitutive equation Eq. (A.2) and dynamic equation Eq. (A.3), the governing wave equations in terms of (\mathbf{u}^s, p) are obtained following [64] as

$$\begin{aligned} & \nabla \cdot \sigma^s (\mathbf{u}^s) + \omega^2 \bar{\rho} \cdot \mathbf{u}^s + \gamma \cdot \nabla p = 0, \\ & \nabla \cdot \left(\frac{1}{\omega^2} \bar{\mathbf{m}}^{-1} \cdot \nabla p \right) + \nabla \cdot (\gamma \cdot \mathbf{u}^s) - \frac{1}{B_8} p = 0, \end{aligned} \quad (5)$$

where

$$\begin{aligned} \sigma^s &= (B_2 - B_6^2/B_8) \nabla \cdot \mathbf{u}^s \cdot \mathbf{I} + 2B_5 \epsilon^s, \\ \bar{\rho} &= \rho \mathbf{I} - \rho_f^2 \bar{\mathbf{m}}^{-1}, \\ \gamma &= \rho_f \bar{\mathbf{m}}^{-1} + B_6/B_8 \mathbf{I}. \end{aligned} \quad (6)$$

here σ^s represents the stress tensor of the solid phase and only depends on \mathbf{u}^s ; $\bar{\mathbf{m}} = \text{diag}[\bar{m}_1, \bar{m}_2, \bar{m}_3]$, $\bar{m}_1 = m_{11} + i r_{11}/\omega$, $\bar{m}_2 = m_{22} + i r_{22}/\omega$, and $\bar{m}_3 = m_{33} + i r_{33}/\omega$. m_{ii} and r_{ii} are coefficients introduced by Biot, and \mathbf{I} is the identity tensor. The weak integrals can be written as

$$\begin{aligned} & \int_{\Omega_p} \sigma^s (\mathbf{u}^s) : \epsilon^s (\delta \mathbf{u}^s) d\Omega - \int_{\Omega_p} \omega^2 \bar{\rho} \cdot \mathbf{u}^s \cdot \delta \mathbf{u}^s d\Omega - \int_{\Omega_p} \gamma \cdot (\nabla p) \cdot \delta \mathbf{u}^s d\Omega \\ & - \int_{S_p} \sigma^s (\mathbf{u}^s) \cdot \mathbf{n}^p \cdot \delta \mathbf{u}^s dS + \int_{\Omega_p} \left(\frac{1}{\omega^2} \bar{\mathbf{m}}^{-1} \cdot \nabla p \cdot \nabla \delta p - \frac{1}{B_8} p \delta p \right) d\Omega \\ & - \int_{\Omega_p} \gamma \cdot \mathbf{u}^s \cdot \nabla \delta p d\Omega + \int_{S_p} \left(\gamma \cdot \mathbf{u}^s \cdot \mathbf{n}^p - \frac{1}{\omega^2} \bar{\mathbf{m}}^{-1} \cdot \nabla p \cdot \mathbf{n}^p \right) \cdot \delta p dS = 0, \end{aligned} \quad (7)$$

where $\delta \mathbf{u}^s$ and δp are test functions for the porous solid displacement \mathbf{u}^s and the pore fluid pressure p , respectively; Ω_p and S_p are the poroelastic domain and its boundary, respectively; and \mathbf{n}^p is the external normal unit vector along the poroelastic medium boundary S_p .

According to the second equation of Eq. (A.2), the relative displacement vector \mathbf{w} can be written in terms of p and \mathbf{u}^s

$$\mathbf{w} = \frac{1}{\omega^2} \bar{\mathbf{m}}^{-1} \cdot \nabla p - \rho_f \bar{\mathbf{m}}^{-1} \cdot \mathbf{u}^s. \quad (8)$$

Furthermore, the relation between the total stress and the solid phase stress is given by Eq. (A.3)

$$\sigma^t = \sigma^s (\mathbf{u}^s) + \frac{B_6}{B_8} p \mathbf{I}. \quad (9)$$

Substituting Eqs. (8) and (9) into Eq. (7), the weak integral form is rewritten as

$$\begin{aligned} & \int_{\Omega_p} \sigma^s (\mathbf{u}^s) : \epsilon^s (\delta \mathbf{u}^s) d\Omega - \int_{\Omega_p} \omega^2 \bar{\rho} \cdot \mathbf{u}^s \cdot \delta \mathbf{u}^s d\Omega - \int_{\Omega_p} \gamma \cdot \nabla p \cdot \delta \mathbf{u}^s d\Omega \\ & - \int_{S_p} \mathbf{n}^p \cdot \sigma^t \cdot \delta \mathbf{u}^s dS + \int_{S_p} \frac{B_6}{B_8} p \delta \mathbf{u}^s \cdot \mathbf{n}^p dS \\ & + \int_{\Omega_p} \left(\frac{1}{\omega^2} \bar{\mathbf{m}}^{-1} \cdot \nabla p \cdot \nabla \delta p - \frac{1}{B_8} p \delta p \right) d\Omega - \int_{\Omega_p} (\gamma \cdot \mathbf{u}^s \cdot \nabla \delta p) d\Omega \\ & + \int_{S_p} \frac{B_6}{B_8} \mathbf{u}^s \cdot \delta p \cdot \mathbf{n}^p dS - \int_{S_p} \varphi (\mathbf{U} - \mathbf{u}^s) \cdot \mathbf{n}^p \cdot \delta p dS = 0, \end{aligned} \quad (10)$$

Applying the divergence theorem and the vector identity [$\nabla \cdot (\alpha \mathbf{v}) = \alpha \nabla \cdot (\mathbf{v}) + \nabla \alpha \cdot \mathbf{v}$], Eq. 10 can be reformulated as [65]

$$\begin{aligned} & \int_{\Omega_p} \sigma^s(\mathbf{u}^s) : \epsilon^s(\delta \mathbf{u}^s) d\Omega - \int_{\Omega_p} \omega^2 \bar{\rho} \cdot \mathbf{u}^s \cdot \delta \mathbf{u}^s d\Omega \\ & + \int_{\Omega_p} \left(-\gamma + \frac{B_6}{B_8} \mathbf{I} \right) \cdot \nabla p \cdot \delta \mathbf{u}^s d\Omega + \int_{\Omega_p} \frac{B_6}{B_8} p \nabla \cdot \delta \mathbf{u}^s d\Omega_p \\ & - \int_{S_p} \mathbf{n}^p \cdot \sigma^t \cdot \delta \mathbf{u}^s dS + \int_{\Omega_p} \left(\frac{1}{\omega^2} \bar{\mathbf{m}}^{-1} \cdot \nabla p \cdot \nabla \delta p - \frac{1}{B_8} p \delta p \right) d\Omega \\ & + \int_{\Omega_p} \left(-\gamma + \frac{B_6}{B_8} \mathbf{I} \right) \cdot \mathbf{u}^s \cdot \nabla \delta p d\Omega + \int_{\Omega_p} \frac{B_6}{B_8} \nabla \cdot \mathbf{u}^s \cdot \delta p d\Omega \\ & - \int_{S_p} \varphi (\mathbf{U} - \mathbf{u}^s) \cdot \mathbf{n}^p \cdot \delta p dS = 0, \end{aligned} \quad (11)$$

The boundary integral is thus $I_p = - \int_{S_p} \sigma^t \cdot \mathbf{n}^p \cdot \delta \mathbf{u}^s dS - \int_{S_p} \varphi (\mathbf{U} - \mathbf{u}^s) \cdot \mathbf{n}^p \cdot \delta p dS$.

3. Interface conditions

In this section, we introduce interface conditions and coupled interface integrals for the following three different combinations: (1) elastic/poroelastic system, (2) acoustic/poroelastic system, and (3) poroelastic/poroelastic system.

3.1. Elastic/poroelastic system

To begin with, we consider the interface between elastic and poroelastic media. In this case, the pore fluid is prevented to flow into the elastic medium at the interface. The solid skeleton and the elastic medium are assumed to be in welded contact. Therefore, the total stress and the displacements are continuous at the interface, and the relative displacement (of the pore fluid with respect to the solid skeleton) vanishes. The corresponding boundary conditions can be expressed as [66]

$$\begin{aligned} \sigma^t \cdot \mathbf{n}^p &= \sigma^e \cdot \mathbf{n}^p, \\ \varphi (\mathbf{U} - \mathbf{u}^s) &= 0, \\ \mathbf{u}^s &= \mathbf{u}^e. \end{aligned} \quad (12)$$

The coupled interface integral (I_{p-e}) is obtained as a combination of the boundary integrals resulting from the weak variational forms of both elastic (I_e) and poroelastic (I_p) domains. It reads as follows:

$$\begin{aligned} I_{p-e} = I_p + I_e &= - \int_{S_{p-e}} \mathbf{n}^p \cdot \sigma^t \cdot \delta \mathbf{u}^s dS - \int_{S_{p-e}} \varphi (\mathbf{U} - \mathbf{u}^s) \cdot \mathbf{n}^p \cdot \delta p dS \\ &+ \int_{S_{p-e}} \mathbf{n}^p \cdot \sigma^e \cdot \delta \mathbf{u}^e dS, \end{aligned} \quad (13)$$

where S_{p-e} represents the interface separating elastic and poroelastic media; and the appearance of the positive sign of the last term is due to the identity $\mathbf{n}^p = -\mathbf{n}^e$ at every point of the interface.

3.2. Acoustic/poroelastic system

Next, we pay attention to the acoustic/poroelastic system with either open- or sealed-pore interfaces. For the open-pore interface, the pore fluid can freely flow in and out of the solid skeleton in the direction normal to the interface. Thus, there is no pressure difference across the interface. The relative mass flux should additionally be conserved. Based on Hamilton's principle [67], the continuity of the total stress is ensured at the interface. Summing up, the interface conditions can be written [44]

$$\begin{aligned} \sigma^t \cdot \mathbf{n} &= -p^a \cdot \mathbf{n}, \\ \frac{1}{\rho_0 \omega^2} \nabla p^a \cdot \mathbf{n} &= (1 - \varphi) \mathbf{u}^s \cdot \mathbf{n} + \varphi \mathbf{U} \cdot \mathbf{n}, \end{aligned}$$

$$p - p^a = 0. \quad (14)$$

For the sealed-pore interface, the pore fluid cannot flow freely in and out of the solid skeleton in a direction normal to the interface. In addition, the acoustic pressure generally will be discontinuous across the interface [15]. Therefore, the interface conditions can be expressed as

$$\begin{aligned} \sigma^t \cdot \mathbf{n} &= -p^a \cdot \mathbf{n}, \\ \frac{1}{\rho_0 \omega^2} \nabla p^a \cdot \mathbf{n} &= (1 - \varphi) \mathbf{u}^s \cdot \mathbf{n} + \varphi \mathbf{U} \cdot \mathbf{n}, \\ (\mathbf{U} - \mathbf{u}^s) \cdot \mathbf{n} &= 0. \end{aligned} \quad (15)$$

The coupled integral (I_{p-a}) on the interface S_{p-a} results from the interaction of fluid and poroelastic media. It reads as follows:

$$\begin{aligned} I_{p-a} = I_p + I_a &= - \int_{S_{p-a}} \mathbf{n}^p \cdot \delta \sigma^t \cdot \mathbf{u}^s dS - \int_{S_{p-a}} \varphi (\mathbf{U} - \mathbf{u}^s) \cdot \mathbf{n}^p \cdot \delta p dS \\ &+ \int_{S_{p-a}} \frac{1}{\omega^2 \rho^a} \nabla p^a \cdot \mathbf{n}^p \cdot \delta p^a dS. \end{aligned} \quad (16)$$

3.3. Poroelastic/poroelastic system

Finally, we consider the poroelastic/poroelastic system with open-pore interfaces. Both media are described in terms of a mixed formulation based on (\mathbf{u}^s, p) . The coupled integral can be obtained as

$$\begin{aligned} I_{p_1-p_2} &= I_{p_1} + I_{p_2} \\ &= - \int_{S_{p_1-p_2}} \mathbf{n}^{p_1} \cdot \sigma_1^t \cdot \delta \mathbf{u}_1^s dS - \int_{S_{p_1-p_2}} \varphi_1 (\mathbf{U}_1 - \mathbf{u}_1^s) \cdot \mathbf{n}^{p_1} \cdot \delta p_1 dS \\ &+ \int_{S_{p_1-p_2}} \mathbf{n}^{p_1} \cdot \sigma_2^t \cdot \delta \mathbf{u}_2^s dS + \int_{S_{p_1-p_2}} \varphi_2 (\mathbf{U}_2 - \mathbf{u}_2^s) \cdot \mathbf{n}^{p_1} \cdot \delta p_2 dS, \end{aligned} \quad (17)$$

where subscripts 1,2 denote the poroelastic media 1 and 2, respectively. Indeed, at the interface $S_{p_1-p_2}$, interface conditions are given by [64]

$$\begin{aligned} \sigma_1^t \cdot \mathbf{n} &= \sigma_2^t \cdot \mathbf{n}, \\ \varphi_1 (\mathbf{U}_1 - \mathbf{u}_1^s) &= \varphi_2 (\mathbf{U}_2 - \mathbf{u}_2^s), \\ \mathbf{u}_1^s &= \mathbf{u}_2^s, \\ p_1 &= p_2. \end{aligned} \quad (18)$$

here the first and second equations denote the continuity of the total stress and relative mass flux across the interface, respectively. The last two equations ensure that the solid skeleton and pore fluid are well connected.

4. Finite element method and geometric model

In this work, we consider three-dimensional (3D) square-lattice metamaterials composed of circular inclusions embedded in a matrix. Either the inclusion or the matrix can be elastic, acoustic, or poroelastic media. \mathbf{n}^m and \mathbf{n}^s are the outward unit normal vectors of the matrix and inclusion at the interface, respectively. The two normal unit vectors point in opposite directions, $\mathbf{n}^s = -\mathbf{n}^m$.

According to Bloch's theorem, both displacements and pressure fields of the harmonic wave read

$$\begin{aligned} \mathbf{u}(\mathbf{r}) &= e^{-i(\mathbf{k} \cdot \mathbf{r})} \mathbf{u}_k(\mathbf{r}), \\ p(\mathbf{r}) &= e^{-i(\mathbf{k} \cdot \mathbf{r})} p_k(\mathbf{r}), \end{aligned} \quad (19)$$

where $\mathbf{k} = (k_x, k_y, k_z)$ is the Bloch wave vector; and $\mathbf{u}_k(\mathbf{r}) = [u_{kx}, u_{ky}, u_{kz}]$ and $p_k(\mathbf{r})$ are periodical functions with the same periodicity as the crystal lattice.

BOFEM is adopted to calculate the complex band structure, by substituting (19) into the wave equation to obtain the general form. As a note, the wave vector is considered the eigenvalue. The general form

$$\mathbf{R}_{a-p} = \begin{bmatrix} 0 \\ 0 \\ 0 \\ -\omega^2 \left[\bar{\mathbf{m}}^{-1} (ik_x p_{\mathbf{k}} + p_{\mathbf{k},x}, ik_y p_{\mathbf{k}} + p_{\mathbf{k},y}, ik_z p_{\mathbf{k}} + p_{\mathbf{k},z}) \cdot \mathbf{n}^a / \omega^2 + (1 - \rho_f \bar{\mathbf{m}}^{-1}) \mathbf{u}_{\mathbf{k}}^s \cdot \mathbf{n}^a \right] \end{bmatrix},$$

Box I.

and interface conditions are combined within the commercial software Comsol Multiphysics to calculate the complex band structure for the different systems. Numerical calculations are implemented using the PDE (Partial Difference Equation) the module of Comsol Multiphysics. The discretized partial differential equations can be written using the following equations system [68]

$$\begin{aligned} \nabla \cdot \mathbf{T} &= \mathbf{G} & \Omega, \\ -\mathbf{n} \cdot \mathbf{T} &= \mathbf{R} & \partial\Omega_N, \\ \mathbf{L} &= 0 & \partial\Omega_L, \end{aligned} \quad (20)$$

where Ω , $\partial\Omega_N$, and $\partial\Omega_L$ are the unit cell domain, Neumann boundary, and Dirichlet boundary, respectively; \mathbf{T} represents the 4×4 equation matrix governing the problem; \mathbf{G} , \mathbf{R} , \mathbf{L} are 4×1 coefficient matrices dependent on variable or its partial derivative and \mathbf{n} is the outward normal unit vector to the interface.

For different systems, the coefficient matrices can be obtained by different interface conditions. \mathbf{T} and \mathbf{G} are determined by the wave equations, respectively. The expressions of coefficient matrices of \mathbf{R} and \mathbf{L} are derived below.

For the elastic/poroelastic system, substituting the third expression of Eq. (12) into Eq. (13), Eq. (13) becomes the equivalent weak integral form of the first and second equations of Eq. (12). This means that the total stress continuity and relative displacement is zero at the interface will be automatically satisfied during the finite element calculation. Therefore, only displacement vector continuity ($\mathbf{u}^s = \mathbf{u}^e$) should be constrained explicitly. Substituting the third equation of Eq. (12) into (20), the coefficient matrix \mathbf{L}_{p-e} can be obtained as

$$\mathbf{L}_{p-e} = \begin{bmatrix} u_{\mathbf{k}x}^e - u_{\mathbf{k}x}^s \\ u_{\mathbf{k}y}^e - u_{\mathbf{k}y}^s \\ u_{\mathbf{k}z}^e - u_{\mathbf{k}z}^s \\ 0 \end{bmatrix}, \quad (21)$$

According to the law of variation $\delta(dq) = d\delta q + q\delta d$, d , q are two dependent variables, and δd , δq are two test functions, respectively. For the acoustic/poroelastic system with the open-pore interface, substituting Eq. (14) into Eq. (16), the coupled integral (I_{p-a}) can be simplified as

$$I_{p-a} = \int_{\Gamma_{p-a}} \delta(p^a \mathbf{u}^s \cdot \mathbf{n}) d\Gamma, \quad (22)$$

The coupled integral Eq. (22) is similar to that of the acoustic-elastic structure [69], so the poroelastic medium will be coupled to the acoustic medium through the classical acoustic-elastic coupling term [65]. In addition, the boundary condition $p=p^a$ also needs to be explicitly imposed on S_{p-a} . Substituting the interface conditions Eq. (14) into Eq. (20), the coefficient matrices \mathbf{R}_{p-a} , \mathbf{R}_{a-p} (see Box I), and \mathbf{L}_{p-a} for an open-pore interface can be obtained as

$$\begin{aligned} \mathbf{R}_{p-a} &= \begin{bmatrix} (p_{\mathbf{k}}^a + B_6 p_{\mathbf{k}} / B_8) n_{\mathbf{k}x}^p \\ (p_{\mathbf{k}}^a + B_6 p_{\mathbf{k}} / B_8) n_{\mathbf{k}y}^p \\ (p_{\mathbf{k}}^a + B_6 p_{\mathbf{k}} / B_8) n_{\mathbf{k}z}^p \\ 0 \end{bmatrix}, \\ \mathbf{L}_{p-a} &= \begin{bmatrix} 0 \\ 0 \\ 0 \\ p_{\mathbf{k}}^a - p_{\mathbf{k}} \end{bmatrix}. \end{aligned} \quad (23)$$

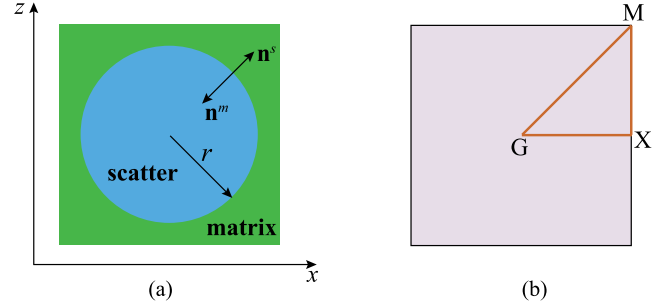


Fig. 1. The 2D square-lattice metamaterial of a circular inclusion embedded in a matrix. (a) Schematic diagram of the unit cell. The metamaterial is assumed infinite along the y -axis and periodic in the (x, z) plane. (b) Sketch of the corresponding first Brillouin zone.

here, \mathbf{R}_{p-a} and \mathbf{R}_{a-p} indicate that the constraints are imposed on the poroelastic domain and acoustic domain, respectively.

For the sealed-pore interface, substituting Eq. (15) into Eq. (16), the coupled integral I_{p-a} is consistent with the open-pore interface. The coefficient matrices \mathbf{R}_{p-a} and \mathbf{R}_{a-p} (see Box II) can be derived as

$$\mathbf{R}_{p-a} = \begin{bmatrix} (p_{\mathbf{k}}^a + B_6 p_{\mathbf{k}} / B_8) n_{\mathbf{k}x}^p \\ (p_{\mathbf{k}}^a + B_6 p_{\mathbf{k}} / B_8) n_{\mathbf{k}y}^p \\ (p_{\mathbf{k}}^a + B_6 p_{\mathbf{k}} / B_8) n_{\mathbf{k}z}^p \\ \rho_f (u_{\mathbf{k}x} n_x / \bar{m}_1 + u_{\mathbf{k}y} n_y / \bar{m}_2 + u_{\mathbf{k}z} n_z / \bar{m}_3) \end{bmatrix}. \quad (24)$$

For the poroelastic/poroelastic system, it should be noted that Eq. (17) is equivalent to the first and second equations of Eq. (18). Therefore, the continuity of both total stress and relative displacement is automatically satisfied. In this case, only $\mathbf{u}_1^s = \mathbf{u}_2^s$ and $p_1 = p_2$ need to be explicitly imposed on S_{p-e} . As a result, the coefficient vector $\mathbf{L}_{p_1-p_2}$ can be obtained as

$$\mathbf{L}_{p_1-p_2} = \begin{bmatrix} u_{2\mathbf{k}x}^s - u_{1\mathbf{k}x}^s \\ u_{2\mathbf{k}y}^s - u_{1\mathbf{k}y}^s \\ u_{2\mathbf{k}z}^s - u_{1\mathbf{k}z}^s \\ p_{2\mathbf{k}} - p_{1\mathbf{k}} \end{bmatrix}. \quad (25)$$

5. Numerical results and discussion

In this section, propagation characteristics of elastic waves in a 2D $x-z$ plane of elastic/poroelastic and fluid/poroelastic metamaterials are investigated. The y -axis is parallel to the invariance axis, and displacements and pressure fields are independent of the y -coordinate ($\mathbf{k}_y=0$). Furthermore, propagation of pure shear wave is neglected for both elastic and poroelastic media, since it only involves the solid skeleton. The geometry considered is depicted in Fig. 1. The lattice constant is $a=2m$ and the radius of the inclusion is $r=0.4a$.

Complex band structures, modal distributions, and transmission spectra are calculated and presented. The influence of elastic material parameters, inclusion radius, and the pore fluid viscosity on dispersion relations and attenuation of the wave is also analyzed. Note that we only discuss wave propagation along the $/X$ direction in the present work. In the following, for convenience, we designate combinations of materials using the letter P for poroelastic, E for elastic, and F for

$$\mathbf{R}_{a-p} = \begin{bmatrix} 0 \\ 0 \\ 0 \\ -\omega^2 \left[\bar{\mathbf{m}}^{-1} (ik_x p_{\mathbf{k}} + p_{\mathbf{k},x}, ik_y p_{\mathbf{k}} + p_{\mathbf{k},y}, ik_z p_{\mathbf{k}} + p_{\mathbf{k},z}) \cdot \mathbf{n}^a / \omega^2 + (1 - \rho_f \bar{\mathbf{m}}^{-1}) \mathbf{u}_{\mathbf{k}}^s \cdot \mathbf{n}^a \right] \end{bmatrix},$$

Box II.

fluid. The combination matrix/inclusion can be either P/E (an elastic inclusion in a poroelastic matrix), E/P (a poroelastic inclusion in an elastic matrix), P/F (a fluid inclusion in a poroelastic matrix), or F/P (a poroelastic inclusion in a fluid matrix). These different cases are treated separately. We also verify the correctness and effectiveness of the formulations established in the paper, see Appendix B for details.

5.1. An elastic inclusion in a poroelastic matrix (P/E system)

First, we consider an elastic inclusion embedded in a poroelastic matrix (poroelastic medium 1), with the geometry shown in Fig. 1(a). Material parameters for the matrix are: $C_{11}=10$ GPa, $C_{12}=2$ GPa, $K_s=2$ GPa, $K_f=2$ GPa, $\rho_s=3000$ kg/m³, $\rho_f=1000$ kg/m³, $\eta=0.0$ Pa/s, $\alpha_1(\infty)=1$, $\alpha_3(\infty)=1$, $\Phi=0.2$, and $d=6.32$ μm. Material parameters for the inclusion (concrete) are: $C_{11}=33.3$ GPa, $C_{12}=8.3$ GPa, and $\rho_s=2500$ kg/m³. The poroelastic medium is isotropic and the pore fluid viscosity is ignored. The complex band structure is shown in Fig. 2(a). The reduced frequency fa is plotted as a function of the reduced wave number $ka/(2\pi)$. Wave polarization is identified by the relative energy ratio between the kinetic energy in the pore fluid and the total kinetic energy in the poroelastic matrix and the elastic inclusion. It is expressed as:

$$P_f = \frac{\int E_k^f dS_1}{\int (E_k^s + E_k^f) dS_1 + \int E_k^e dS_2}. \quad (26)$$

here $E_k^e = \rho_e \omega^2 (u_x^2 + u_z^2)/2$, $E_k^s = (1 - \varphi) \rho_s \omega^2 (u_x^2 + u_z^2)/2$, and $E_k^f = \varphi \rho_f \omega^2 (U_x^2 + U_z^2)/2$ are the kinetic energy for the elastic inclusion, the pore solid skeleton, and the pore fluid, respectively. S_1 and S_2 represent the matrix and inclusion domains, respectively.

To compare with the dispersion relation, we also calculate the transmission spectrum for a finite structure with 50 unit cells. Three different excitation signals, $(u_{x0}, u_{y0}, p_0) = (1, 0, 0)$, $(0, 1, 0)$, and $(0, 0, 1)$, are applied to the left side of the finite structure. The transmitted signal is detected on the right side of the structure. Continuous boundary conditions are applied to the upper and lower surfaces. The frequency response is defined as

$$T = \log_{10} \left(\frac{\int U_R dl}{\int U_0 dl} \right), \quad (27)$$

where $U_R = |u_x|$ or $|u_y|$ or $|p|$ and $U_0=1$ are the amplitudes of the received and incident signals, respectively. As a note, $l=a$ is the length of the line for recording the transmitted signal.

As a reference, the complex band structure for the P/P system with the open-pore interface is plotted with black points. This system is obtained by replacing the elastic inclusion with the poroelastic medium 2, considering the same solid skeleton parameter, whereas the pore fluid is the same as for the matrix. Unlike the wavenumber band gap of 2D FSPMs [50], an avoided crossing is formed at low frequencies in this work. The avoided crossing is characterized by real parts of the bands avoiding each other [70]. This characteristic is similar to the anticrossing of photon-magnon coupling which is formed due to coherent interaction between microwave optical photons and spin systems [71].

For the P/E system, the fast-longitudinal (P_1) and slow-longitudinal (P_2) waves are distinguished by color varying from blue (0) to red (1). Anyway, these longitudinal waves interact and hybridize. Compared

with the P/P system, it is clear that three waves have smaller phase velocities. Especially, the decreasing of the P_2 wave is the most remarkable. The first band gap of the P_2 wave is also widened from 375 m/s to 740 m/s. We find that a wavenumber band gap [72] appears at low frequencies ($fa=800$ m/s). The wavenumber band gap is characterized by real parts of bands moving toward each other and converging [70]. This characteristic is similar to the opposite anticrossing of photon-magnon coupling generated by the compensation of both intrinsic damping and coupling-induced damping of magnon modes [73].

Another striking phenomenon is the emergence of a complete band gap between 1170 m/s and 1200 m/s and of flat bands around $fa=1180$ m/s. For clarification, the zoomed complex band structure and transmission spectrum in reduced frequency regions 1130 m/s–1230 m/s and 1130 m/s–1450 m/s are displayed in Fig. 2(c–f). We can see that the frequency response decreases very quickly and that transmission dips are very sharp for all three waves [Fig. 2(d)]. Interestingly, the transmission of the SV wave shows the same trend as transmissions of two longitudinal waves, which is not obvious from the observation of the imaginary parts of the complex band structure. Modal distribution at marked points (N_1 – N_5) in Fig. 2(c,e) are shown in Fig. 3. It is observed that the vibration mode at the marked point N_5 is mainly dominated by the pore fluid displacement, and displacement polarization $P_d = |u_y|/|U|$ is 1:7. This means that when the SV wave is selected as the source signal, the P_2 wave will also be excited. Therefore, the response is the result of the coupling of two waves. It is also seen that the transmission dip for the SV wave is deeper than that for two longitudinal waves since the minimum imaginary part of the SV wave is larger. Thus, the displacement along the x -direction of point N_4 decays slower than that of point N_5 .

It is worth pointing out that generation mechanisms for band gaps are different between the SV wave and two longitudinal waves. For the SV wave, it is easily found that the continuity of the second branch is broken and a π phase jump exists. This is known as the local resonance band gap [74], formed from the hybridization between a local resonance and the continuous Bloch wave. It is clearly observed that the vibration at the N_2 and N_5 points is localized in the matrix, and that the displacement component in the pore fluid is much larger than in the solid skeleton and in the elastic inclusion. Therefore, hybridization occurs in the pore fluid. The corresponding band gap is narrow, so hybridization is weak.

For two longitudinal waves, it can be also seen from Fig. 2(e) that the P_1 wave and the P_2 wave intersect at point D_1 and form an evanescent wave EP₁₂. Imaginary parts first increase with frequency and then separate at point D_2 . It is observed that the imaginary part of the P_1 wave gradually decreases, but that of the P_2 wave gradually increases from point D_2 . Thus, the trajectory of the imaginary part has

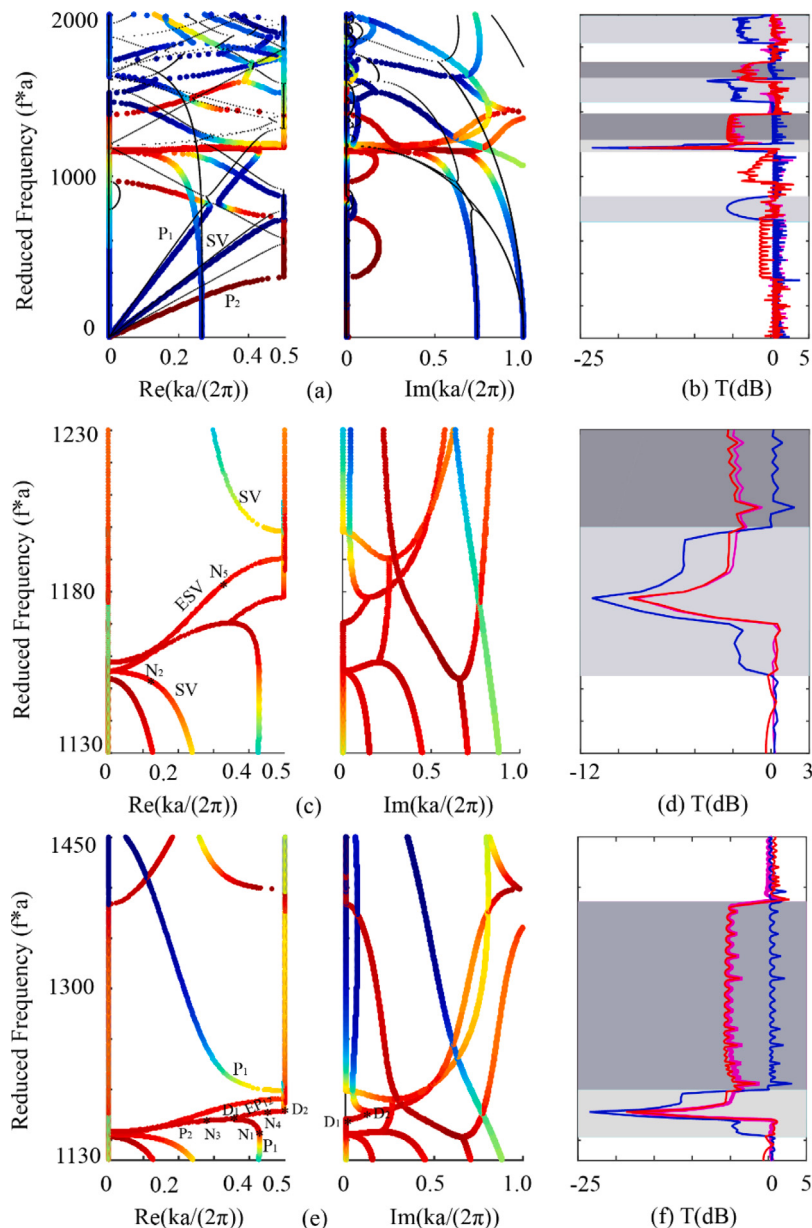


Fig. 2. Complex band structures and transmission spectra for the P/E system (an elastic inclusion in a poroelastic matrix). Panel (a) consists of two parts: the left and right parts show the relation of the reduced frequency with the real and imaginary parts of the wave number, respectively. The color scale indicates wave polarization varying from blue (0) to red (1). Black dots are for the complex band structure of the P/P system with the open-pore interface. Panel (b) shows the transmission spectrum of a finite structure with 50 unit cells. The red, blue, and pink solid lines are for the responses to incident signals $(1, 0, 0)$, $(0, 1, 0)$, and $(0, 0, 1)$, respectively. Light gray regions represent band gaps for longitudinal waves. Panels (c–f) are zoomed complex band structures and transmission spectra in the reduced frequency regions 1130 m/s–1230 m/s and 1130 m/s–1450 m/s.

a cusp. At the same time, the frequency response [Fig. 2(f)] rapidly decreases to form a transmission dip at which the imaginary part reaches the maximum value. These traits are similar to local resonance band gaps [75]. There are further differences when the imaginary part does not reduce to zero. Modal vibration (Fig. 3) at marked points (N_1 , N_3 , N_4) is similar to that of the SV wave at point N_5 . Modal vibration is dominated by the pore fluid, and the vibration of the porous solid can almost be ignored. This also leads the relative energy ratio (P_f) of the P_1 wave to approach 1. In addition, the ‘quasi-resonance Bragg’ band gap [76] is found. It is formed by the overlapping between the first Bragg band gap and the local resonance band gap of the P_1 wave. Hence, compared with the result of the P/P system, the lower boundary of the first band gap of P_1 waves moves down in frequency and the band gap widens. These have not been observed in previous work on the fluid-saturated periodic porous medium [49–51]. It is worth

emphasizing that there is no separate local resonance band gap in the poroelastic matrix because resonances emerge only after introducing the elastic and poroelastic interface.

5.2. A poroelastic inclusion in an elastic matrix (E/P system)

Next, we consider wave propagation in the E/P system. Material and geometric parameters are consistent with those described above. Results are shown in Fig. 4(a,b). Wave polarization is now expressed as $P_{fe} = \int \rho_e \omega^2 u_x^2 / 2dS_1 / \int \rho_e \omega^2 (u_x^2 + u_z^2) / 2 dS_1$. The color scale varies from red to blue, representing the change of wave polarization from longitudinal to shear. Two different wave sources $(u_{x0}, u_{z0}) = (1, 0)$ and $(0, 1)$ are considered. The frequency response is now defined as $T = \log_{10}(\int U_R dl / \int U_0 dl)$, where $U_R = |u_x|$ and $U_0 = 1$ are the amplitudes of the received and incident signals. As a reference, we also plot the

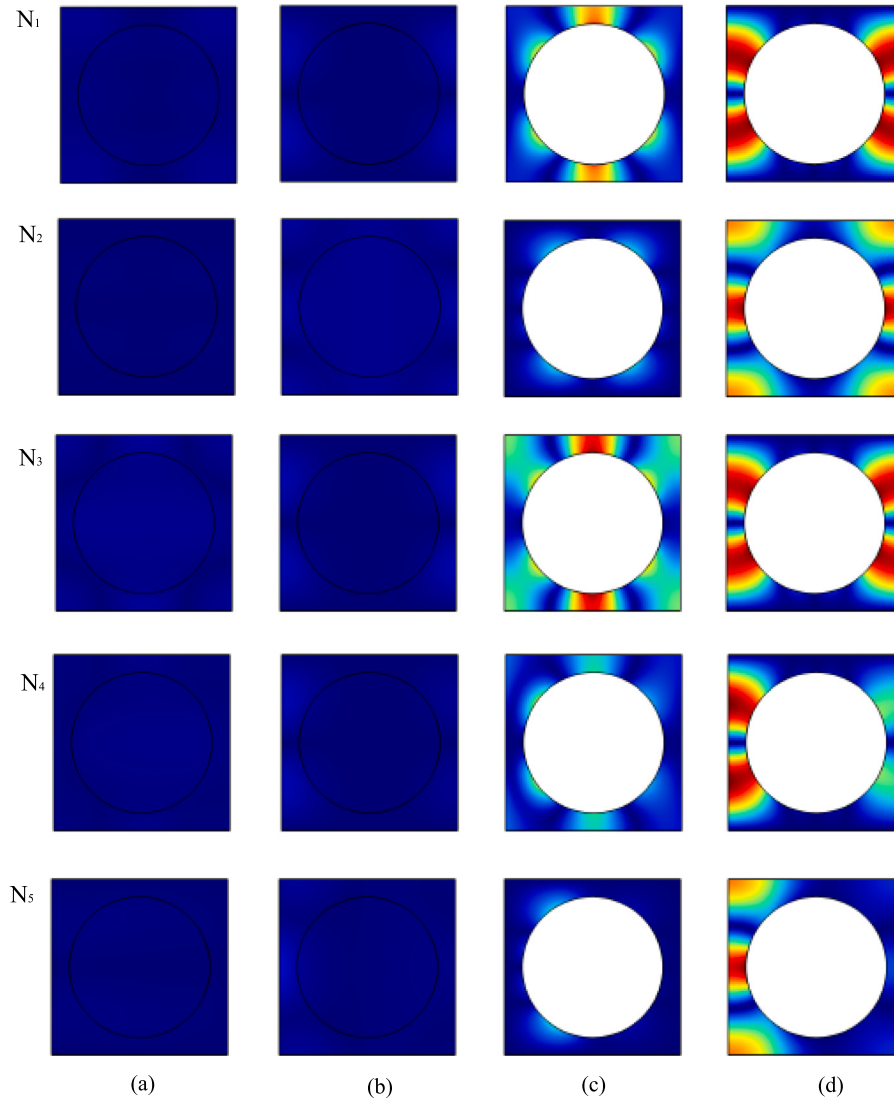


Fig. 3. Modal distributions at marked points (N_1, N_2, N_3, N_4, N_5) in Fig. 2(a). Panels (a), (b), (c), and (d) show normalized displacements $|u_x|/u_{\max}$, $|u_z|/u_{\max}$, $|U_x|/u_{\max}$, and $|U_z|/u_{\max}$, respectively. $u_{\max} = \max(|u_x|, |u_z|, |U_x|, |U_z|)$ at every marked point. The color scale represents the normalized displacement amplitude ranging from 0 (blue) to 1 (red).

real band structure for the solid/solid structure with black dots. This computation is achieved by replacing the poroelastic inclusion with an elastic inclusion similar to the porous solid skeleton. Compared with the result of the solid/solid system, it is noted that flat bands appear around $f a=840$ m/s and 1350 m/s. For clarity, zoomed complex band structures and transmission spectra are shown for reduced frequency ranges 780 m/s–900 m/s and 1200 m/s–1500 m/s in Fig. 4(c–f). It is clearly seen from Fig. 4(c,d) that a pass band (780 m/s–900 m/s) for SV waves appears inside the first Bragg band gap for the SV wave of the solid/solid result. Modal distributions at marked points O_1 – O_5 are illustrated in Fig. 5. It can be seen that the vibration at O_3 and O_4 points is concentrated in the inclusion. Furthermore, displacement distributions in the pore fluid at points O_3 and O_4 are similar. We emphasize that flat bands are associated with the resonance of the inclusion. Meanwhile, they appear owing to the introduction of the elastic and poroelastic interface.

Another observed feature is that the continuity of the first branch for the P wave is broken and a low-frequency band gap (800 m/s–870 m/s) is formed. Modal distributions at marked points (O_1, O_2, O_5) are concentrated on the inclusion. And, the distribution of U_x and

U_z is similar. Thus, this is again a local resonance band gap. Different from the P/E case, the locally resonant band gap opens up as a result of the interaction between locally resonant modes of the poroelastic inclusion and of longitudinal waves propagating in the matrix [74]. That interaction, in turn, leads to a flattening of branches at intersections and reduction in the group velocities [77]. Surprisingly, transmission is not in direct relation with the imaginary part of the P wave, and there is no transmission dip as observed for traditional local resonance band gaps [75,78]. Calculated displacement polarization ($P_d = |u_x|_{\max}/|u_z|_{\max}$) in the matrix at points O_2 is 5:1. This means that when the P wave is selected as the wave source, the SV wave will also be excited. As a consequence, interference between the P wave and SV wave occurs [79] and the frequency response is similar to the minimum imaginary part among P and SV waves. The zoomed complex band structure and transmission spectrum for the reduced frequency range 1200 m/s–1500 m/s also show similar characteristics. A local resonance band gap for SV waves forms and a pass band for P waves appear inside the Bragg band gap for P waves of the solid/solid system, because of the existence of the elastic and poroelastic interface. In addition, a complete band gap (1335 m/s–1342 m/s) with a very large value of the transmission dip appears.

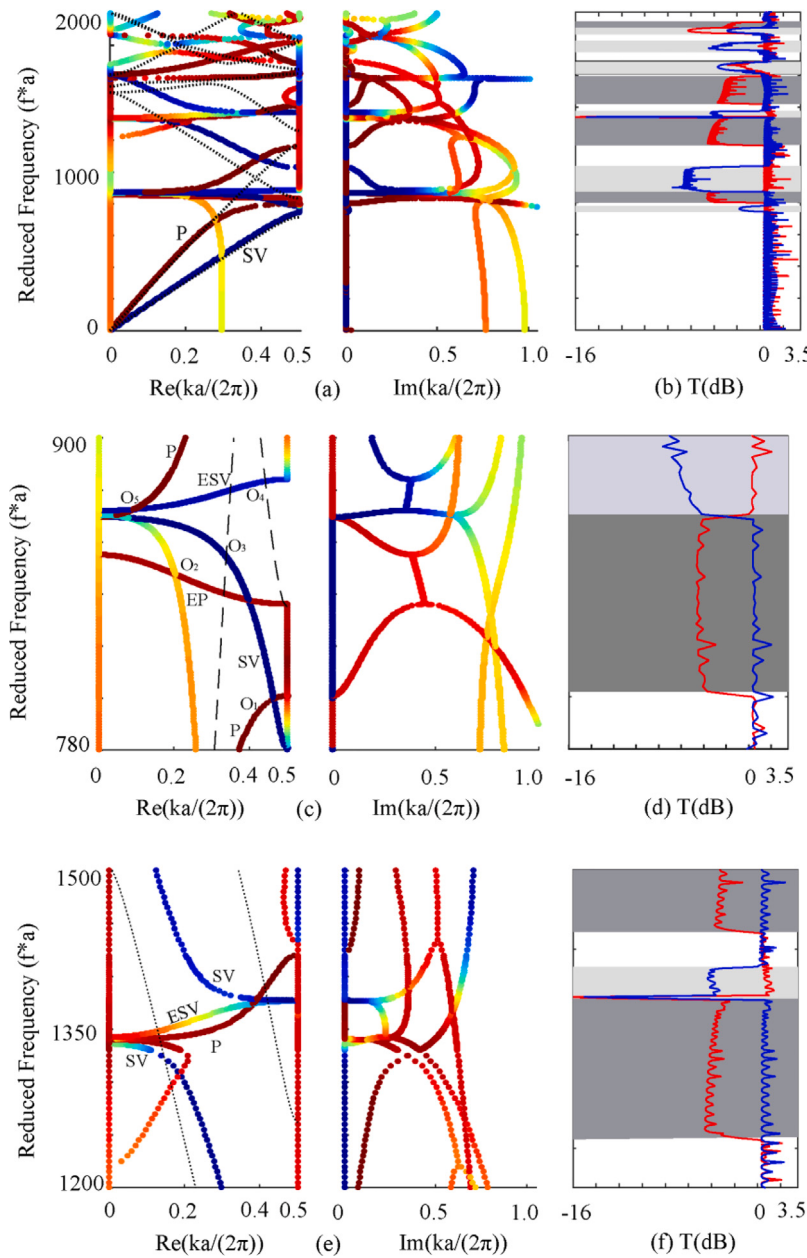


Fig. 4. Complex band structures and transmission spectra for the E/P system (a poroelastic inclusion in an elastic matrix). Panel (a) shows the complex band structure or the dependence of the reduced frequency with the real and imaginary parts of the wave number. Black dots represent the real band structure of a 2D solid/solid structure with constant geometric parameters. The color scale indicates the ratio of the kinetic energy in the x direction to the total kinetic energy in the matrix, ranging from 0 (blue) to 1 (red). Light gray regions represent band gaps for SV waves, whereas gray regions represent band gaps for P waves. Panels (c) and (e) are zoomed complex band structures, and panels (d) and (f) are zoomed frequency responses of panels (a) and (b), for reduced frequency ranges 780 m/s–900 m/s and 1200 m/s–1500 m/s, respectively.

5.3. Parametric study

The dispersion relation is strongly affected by material and geometric parameters. Hence, we examine the influence of material properties and inclusion radius on wave propagation for the P/E and the E/P systems. Results are presented in Figs. 6 and 7.

For the P/E system, when the radius is decreased from $r=0.4a$ [Fig. 2(a)] to $0.2a$ [Fig. 6(a)], the wavenumber band gap at low frequencies becomes an avoided crossing around $fa=750$ m/s. But a wavenumber band gap appears around $fa=1050$ m/s. A similar change can be achieved by the rotation of a YIG sphere, in which case both an avoided crossing and a wavenumber band gap can be observed [80]. The phase velocity of the P_2 wave obviously becomes large since the interference wavelength in the structure is decreased [81]. The first Bragg band gap is narrowed as Bragg scattering in the PC

becomes weak [82]. No complete band gap is found. When the inclusion is replaced with epoxy [Fig. 6(c)], the material parameters are: $C_{11}=10.454$ GPa, $C_{12}=1.59$ GPa, $\rho_s=1180$ kg/m³. There is also in this case an avoided crossing around $fa=750$ m/s, similar to locking in the presence of weak coupling [83]. The first branch of the P_1 wave is broken by the flat band at $fa \approx 1150$ m/s. If aluminum ($C_{11}=125.7$ GPa, $C_{12}=68.3$ GPa, $\rho_s=2730$ kg/m³) is selected instead of epoxy (Fig. 6(e)), a wavenumber band gap is produced at low frequencies ($fa \approx 830$ m/s), similar to the concrete result in Fig. 2(a). Two complete band gaps are generated. At the same time, a quasi-resonance Bragg band gap also forms at $fa \approx 1200$ m/s. Therefore, these reveal that the larger radius and the stiffer inclusion, the more favorable it is to generate the wave number and the ‘quasi-resonance Bragg’ band gaps.

Fig. 7 presents complex band structures and frequency responses for the E/P system, for different material and geometrical parameters.

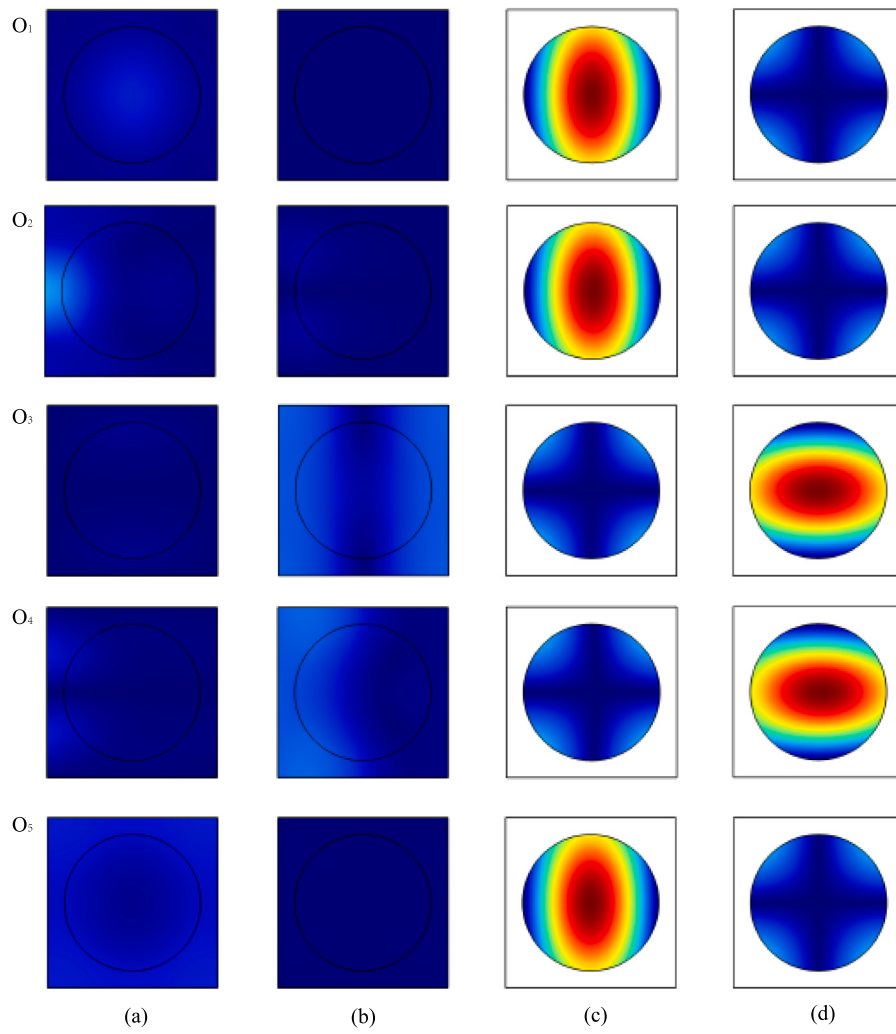


Fig. 5. Modal distributions at marked points (O_1, O_2, O_3, O_4, O_5) in Fig. 4(c). Panels (a), (b), (c), and (d) show normalized displacements $|u_x|/u_{\max}$, $|u_z|/u_{\max}$, $|U_x|/u_{\max}$, and $|U_z|/u_{\max}$, respectively. $u_{\max} = \max(|u_x|, |u_z|, |U_x|, |U_z|)$ at every marked point. The color scale is the same as in Fig. 3.

If $r/a=0.2$, in comparison with Fig. 4(a), the phase velocity of two longitudinal waves obviously becomes large and flat bands move to higher frequencies. Two complete band gaps are formed at $fa \in 1634$ m/s– 1688 m/s and 1852 m/s– 1960 m/s. When the radius is constant ($r=0.4a$) and concrete is replaced by the epoxy, the local resonance band gap of the P wave is widened. A complete band gap [Fig. 7(d)] around $fa=885$ m/s is produced since the P and SV bang gaps overlap. The corresponding frequency response shows a deep transmission dip. When concrete is replaced with aluminum, the result is similar to Fig. 4(a). The first locally resonant band gap for the P wave is relatively narrow because of strong hybridization [74]. Furthermore, there is a pass band for the SV wave inside the first local resonance band gap for the P wave. There are, however, also differences with the concrete matrix [Fig. 4(a)]. A complete band gap is found at low frequencies (812 m/s–865 m/s). It can be concluded that the softer the elastic material, the more favorable it is to forming a complete band gap. The harder the elastic material, the more likely the pass band of the SV wave will appear inside the locally resonant band gap for the P wave.

5.4. A fluid inclusion in a poroelastic matrix (P/F system) with the open-pore interface

Now, we study wave propagation in the P/F system with the open-pore interface. For the matrix, we take the same parameter for the

poroelastic medium as for the P/E system. The fluid in the inclusion is water, whose density and velocity are $\rho_w=10^3$ kg/m³ and $c_w=1490$ m/s, respectively. The complex band structure and the transmission spectrum are presented in Fig. 8. Wave polarization is defined as the energy ratio between the kinetic energy in the pore fluid and the total kinetic energy in the poroelastic matrix $P_f=\int E_k^f dS_1/\int (E_k^s + E_k^f) dS_1$. For comparison, the real part of the complex band structure for the P/E system is also plotted with black dots. It is observed that phase velocities of the P_2 and SV waves for the P/F system are smaller than for the P/E system, since the interference wavelength of multiple Bragg scattering in the structure is increased [81]. Neither a wavenumber band gap nor an avoided crossing is observed, but two complete band gaps are formed in reduced frequency ranges 400 m/s–820 m/s and 1150 m/s–1350 m/s. Another remarkable feature in Fig. 8(a) is that the cut-off frequency for the P_1 wave emerges around $fa=845$ m/s owing to the introduction of the fluid and poroelastic interface. This may be associated with the free flow of fluid across the continuous interface and the coupling of the displacement between pore fluid and water [44]; however, it is not related to periodicity [84]. In theory, the P_1 wave within the cut-off band gap should be fully suppressed [85]. In fact, however, attenuation is seen only when band gaps for both P_1 and P_2 waves overlap, since wave equations for two longitudinal waves are generally coupled. As seen in Fig. 8(a), the overlapping band gap range from the highest point Q_1 ($fa=540$ m/s) of the first branch of the P_2 wave to the cut-off frequency point Q_2 ($fa=615$ m/s) of the P_1

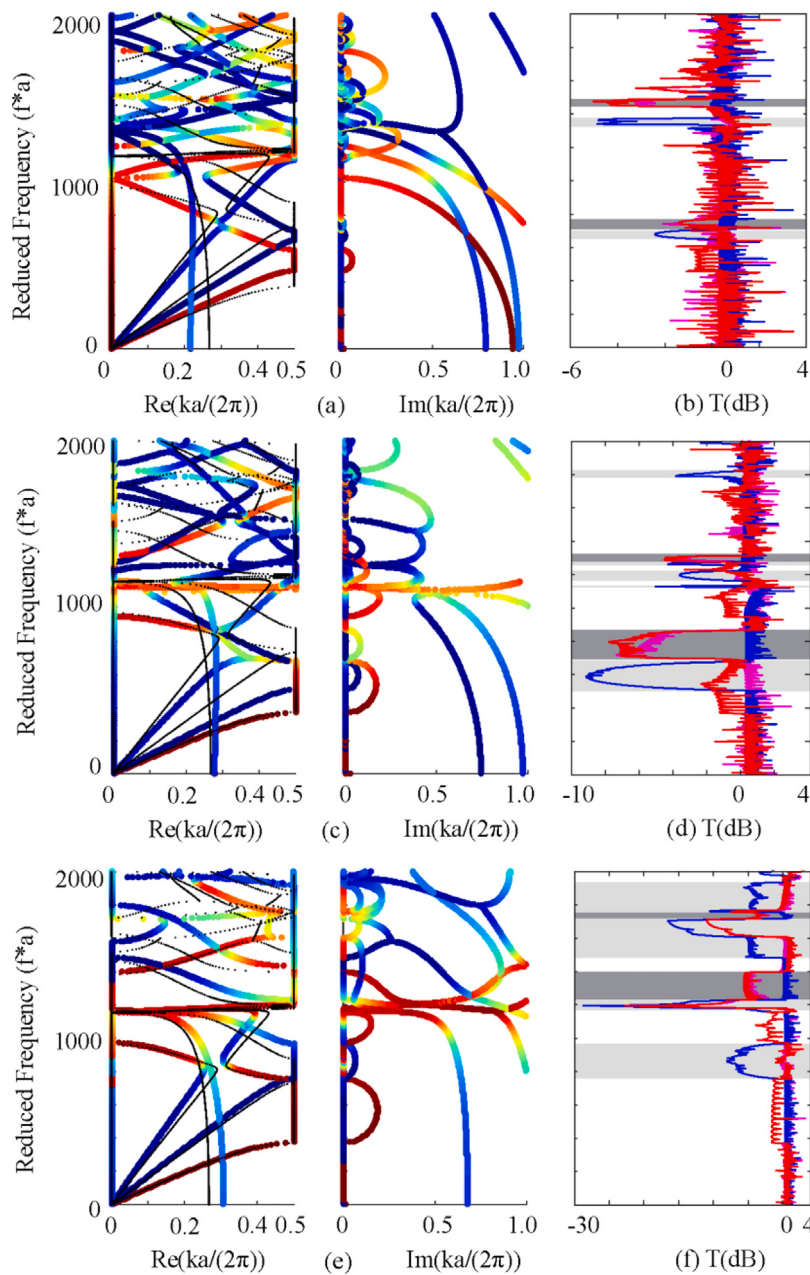


Fig. 6. Influence of the normalized radius r/a and elastic material parameters on the complex band structure and the frequency response for the P/E system (an elastic inclusion in a poroelastic matrix). Panels (a,b) present results for $r/a=0.2$. Panels (c,d) and (e,f) present results for epoxy and aluminum, respectively. Black dots are real parts of the complex band structure for the concrete inclusion [Fig. 2(a)]. The color scale indicates wave polarization varying from blue (0) to red (1). The red, blue, and pink solid lines are for transmission responses to incident signals $(1,0,0)$, $(0,1,0)$, and $(0,0,1)$, respectively. Light gray regions represent the band gaps for the SV wave in the complex band structure, whereas gray regions show the band gaps for the two longitudinal waves.

wave. Surprisingly, the phase velocity of the SV wave is even smaller than that of the P_2 wave. This result is somewhat counterintuitive and has not been observed before to the best of our knowledge.

5.5. A poroelastic inclusion in a fluid matrix (F/P system) with the open-pore interface

The complex band structure and the transmission spectrum for the F/P system with the open-pore interface are presented in Fig. 9. Material and geometric parameters are again consistent with the P/F system. As a reference, the real part of the complex band structure for the fluid/solid structure is plotted with black dots. The latter case is obtained by substituting the poroelastic inclusion with the elastic solid, considering parameters of the porous solid skeleton. Wave polarization

is defined as the energy ratio between the kinetic energy in the pore fluid and the total kinetic energy of the poroelastic inclusion. It is worth pointing out that the dispersion relation is strongly dependent on the properties of the inclusion. Compared with the fluid/solid system, the phase velocity is higher for the F/P system since the poroelastic inclusion is softer [86]. A pass band FP_1 [Fig. 9(a)] appears inside the band gap and transmission is smaller than that of other pass bands [Fig. 9(b)] due to the vibration of the unit cell mainly concentrated on the matrix. There are two narrow band gaps in the ranges 944 m/s–948 m/s and 1276 m/s–1279 m/s, and corresponding frequency responses quickly weaken and transmission dips are very deep. To illustrate the physical mechanism of their formation, zoomed complex band structures and frequency responses are shown in Fig. 9(c–f). It is observed that the variation of the imaginary parts of the bands [Fig. 9(c,e)] and the

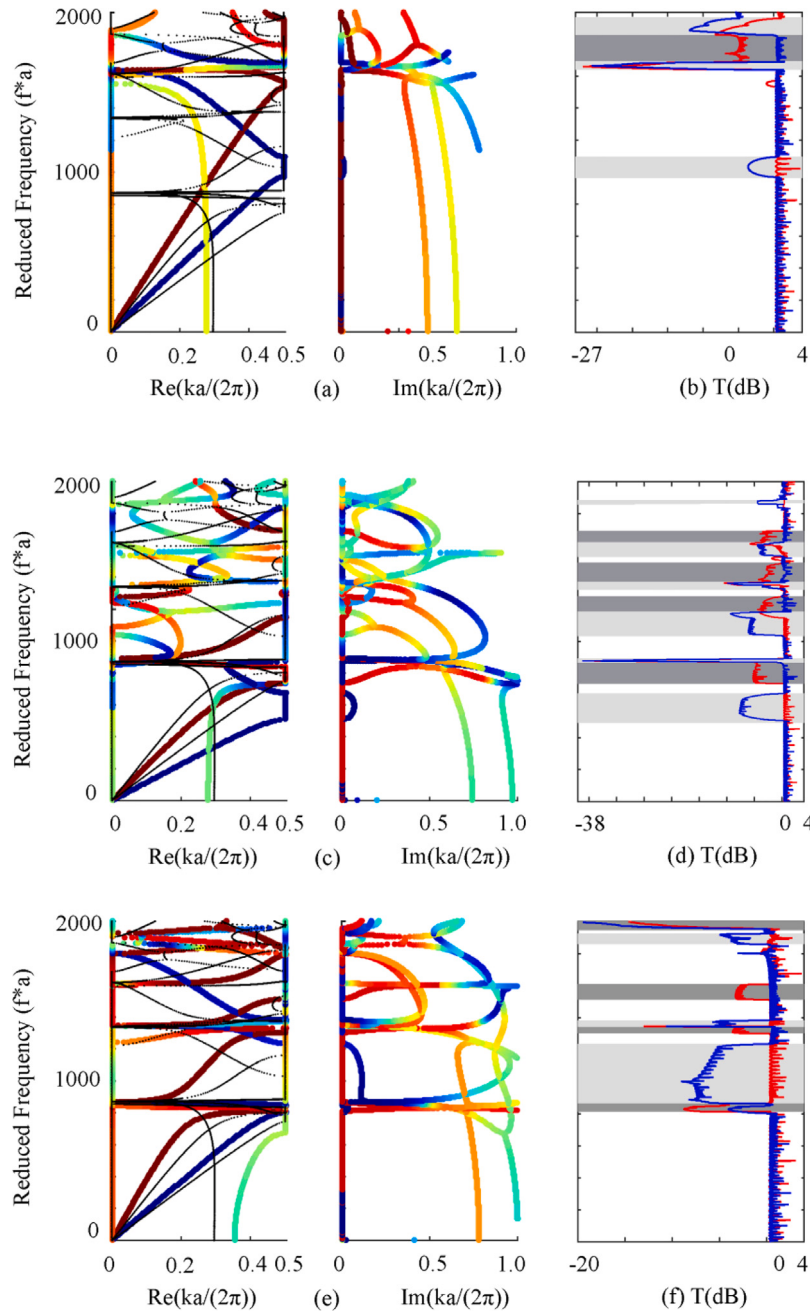


Fig. 7. Influence of normalized radius r/a and elastic material parameters on the complex band structure and the frequency response for the E/P system (a poroelastic inclusion in an elastic matrix). Panels (a,b) present results for $r/a=0.2$. Panels (c,d) and panels (e,f) present results for epoxy and aluminum for $r/a=0.4$. Black points are real parts of the complex band structure for the concrete matrix [Fig. 4(a)]. The color scale indicates wave polarization varying from blue (0) to red (1). Light gray regions represent band gaps for SV waves, whereas gray regions represent band gaps for P waves.

frequency responses [Fig. 9(d,f)] inside the first and the second narrow band gaps are similar to those of Bragg and local resonance band gaps [58], respectively. These results are associated with the fluid and poroelastic interface. In addition, we also pick out points Q_3 and Q_4 from Fig. 9(c,e) and calculate modal distributions, as shown in Fig. 10. It is observed that vibration at two points is mainly dominated by the pore fluid. Furthermore, it is interesting to find that the displacement distribution in the unit cell is symmetric about the center. Therefore, we guess that resonance bands LR_1 and LR_2 [Fig. 9(a)] may be related to the vibration of the pore fluid.

5.6. A fluid inclusion in a poroelastic matrix (P/F system) with the sealed-pore interface

Wave propagation through the P/F system with the sealed-pore interface is investigated. Complex band structures and transmission spectra are presented in Fig. 11. Wave polarization is the same as for the open-pore interface. Compared with the result for the open-pore interface, the most pronounced difference is that the cut-off frequency of the P_1 wave is not observed. An avoided crossing [Fig. 11(a)] is found and it is much wider than the open-pore case owing to the stronger coupling between the porous solid skeleton and pore fluid [44]. It also can be seen from Fig. 11(b) that two complete band gaps are

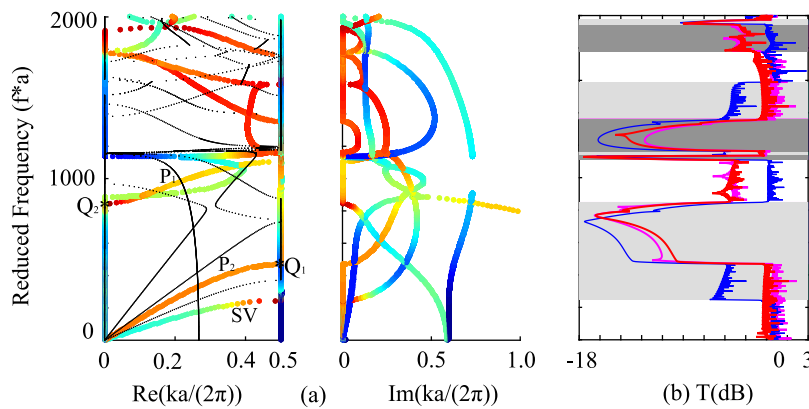


Fig. 8. Complex band structure and transmission spectrum for the P/F system (a fluid inclusion in a poroelastic matrix) with the open-pore interface. The left and right parts in panel (a) stand for the relation of the reduced frequency with the real and imaginary parts of the wave number. The color scale indicates the ratio of the kinetic energy of the pore fluid to the total kinetic energy in the matrix, ranging from 0 (blue) to 1 (red). Black dots are the real part of the complex band structure for the P/E system. The calculated transmission spectrum is plotted in panel (b). The red, blue, and pink solid lines are for responses to incident signals $(1,0,0)$, $(0,1,0)$ and $(0,0,1)$, respectively. Light gray regions represent band gaps for SV waves, whereas gray regions represent band gaps for P waves.

formed between 883 m/s–908 m/s and 1214 m/s–1248 m/s. Zoomed complex band structures and frequency responses (700 m/s–1000 m/s and 1050 m/s–1300 m/s) are depicted in Fig. 11(c–f). It is obviously observed that the first complete band gap is produced because the SV wave becomes the evanescent SV wave from point Q_5 ($f/a = 803$) inside the avoided crossing of two longitudinal waves. In addition, transmission [Fig. 11(d)] of the longitudinal waves is smaller than that of the SV wave. However, the zoomed complex band structure at high frequency [Fig. 11(e)] is too complicated to distinguish characteristics of waves. Similar to the open-pore case, the phase velocity of the SV wave is still smaller than that of the P_2 waves.

5.7. A poroelastic inclusion in a fluid matrix (F/P system) with the sealed-pore interface

Fig. 12 reports the complex band structure and the transmission spectrum for the F/P system with the sealed-pore interface. As a reference, the real part of the complex band structure for the open-pore interface is also plotted with black dots. Wave polarization is defined as for the open-pore case. Compared with the open-pore interface, it is seen that the first branch of the real part almost coincides for both cases. This implies that the interface has little effect at low frequencies. However, this band is lower for the sealed-pore case when it closes to the right boundary. This observation suggests that the phase velocity becomes small and that the effective density of the phononic state becomes large. Furthermore, mode interference is strengthened [87]. In addition, the resonant bands move down in frequency and the transmission dip [Fig. 12(b)] becomes deeper than that of the open-pore interface. Polarization of the flat band approaches 1 which means that the vibration of the inclusion is concentrated on the pore fluid. We also calculate the vibration distribution of the inclusion at point Q_6 in Fig. 13. Obviously, the displacement of the porous solid is much smaller than that of the pore fluid.

5.8. Influence of radius for the P/F system

We have also checked the influence of the radius r of the inclusion on the propagation of elastic waves for the P/F system with the open- and sealed-pore interfaces. Calculated results are gathered in Figs. 14 and 15, respectively. For the open-pore interface, with an increase in the radius, the cut-off frequency for the P_1 wave increases. The cut-off frequency increasing with varying material parameters has been reported in photonic crystals modeled as a metal-infiltrated opal [88]. Only a complete band gap appears in Fig. 14(b), but two complete band

gaps are formed in Fig. 14(d). We can also find that the avoided crossing becomes narrow when the radius is increased. Our study further confirms that the cut-off frequency is associated with the connectivity of the interface [89]. Different from the results for the P/E system in Fig. 3(a) and 6(a), however, the band edge of the first branch for SV waves moves down faster than for P waves as the radius is increased. Furthermore, when the radius is $r=0.3a$ [Fig. 14(c)], the phase velocity of the SV wave smaller than that of the P_2 wave is found.

For the sealed-pore interface, when the radius is $0.2a$ [Fig. 15(a)], the first branches of the dispersion relation of the P_2 and SV waves coincide. Two narrow complete band gaps (around $f/a=625$ m/s and 1830 m/s) are observed in Fig. 15(b). Increasing the radius to $0.3a$ [Fig. 15(c)], the first branches of the P_2 and SV waves are separated and the phase velocity of the SV wave is smaller than that of the P_2 wave. It is consistent with that of the open-pore interface. At the same time, two complete band gaps [Fig. 15(d)] are generated in reduced frequency ranges 540 m/s–580 m/s and 1030 m/s–1130 m/s, and the frequency response [Fig. 15(d)] of the second complete band gap is very small. It is also observed that the phase velocity of the P_1 wave is weakly dependent on the radius of the inclusion.

5.9. Effects of pore fluid viscosity

The effects of the pore fluid viscosity on wave propagation in poroelastic media is also of importance [90,91], since it makes wave propagation dispersive and energy dissipative. In the following, the pore fluid viscosity is introduced to analyze its influence on wave characteristics. The calculated results are further compared to results for the inviscid pore fluid. Geometrical and material parameters are otherwise the same as those for metamaterials with an inviscid pore fluid of the previous sections.

5.9.1. The P/E and E/P systems

Firstly, we pay attention to the effect of the pore fluid viscosity on wave propagation for the P/E system. Fig. 16(a,b) show the dispersion relation and the transmission spectrum for a small viscosity ($\eta = 1 \times 10^{-7}$ Pa s). As a reference, the complex band structure for the inviscid pore fluid is plotted with black dots. Sharp corners of the real part at high-symmetry points of the Brillouin zone become rounded, as reported earlier [92]. Interestingly, real parts of the wavenumber band gap begin to approach each other and imaginary parts become non-zero. At the same time, a slight attenuation is also seen in the frequency response [Fig. 16(b)]. Inside the complete band gap, from 1130 m/s to 1230 m/s, the real and imaginary parts of degenerated evanescent waves EP₁₂ are completely separated. In addition, the cusp

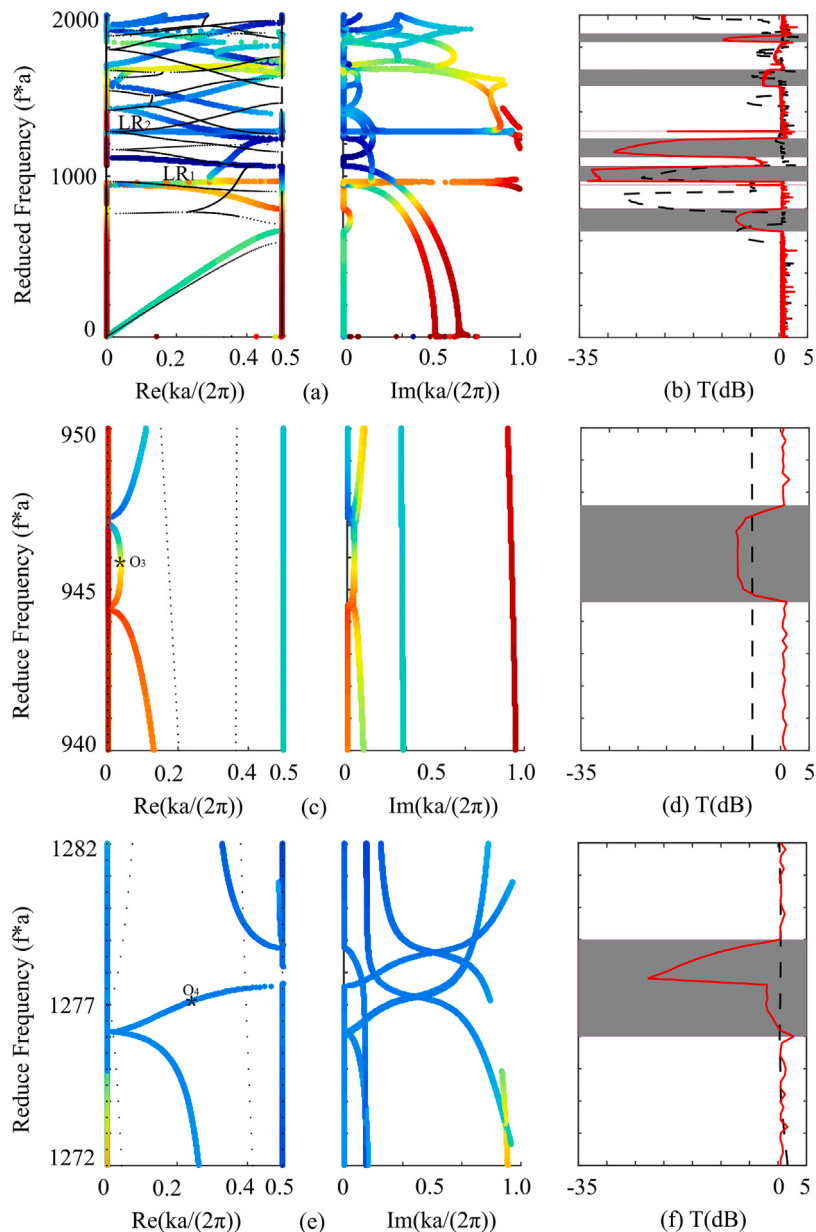


Fig. 9. Complex band structure and transmission spectrum for the F/P system (a poroelastic inclusion in a fluid matrix) with the open-pore interface. The left and right parts in panel (a) stand for the relation of the reduced frequency with the real and imaginary parts of the wave number. The color scale indicates the ratio of the kinetic energy of the pore fluid to the total kinetic energy of the inclusion, from 0 (blue) to 1 (red). Black dots present the real part of the complex band structure of the associated 2D fluid/solid system with solid skeleton parameters of the poroelastic inclusion used for the solid. The calculated transmission spectrum is plotted in panel (b). Red solid lines present the received signal $\log_{10} |p|$ under the unit excitation ($p_0=1$). Black dashed lines present the transmission of the fluid/solid system. Gray regions indicate band gaps for longitudinal waves. Panels (c–f) are zoomed complex band structures and transmission spectra in the reduced frequency regions 940 m/s–950 m/s and 1272 m/s–1282 m/s.

of the imaginary part is not observed and the transmission dip inside the quasi-resonance Bragg band gap also disappears. Inside the local resonance band gap for the SV wave, the imaginary part becomes smaller, which contributes to the propagation of elastic waves. As a result, the transmission dip in the frequency response becomes even shallower and smoother. This is significantly contrary to the previous result of two fluid-saturated porous metamaterials [50] due to the introduction of the poroelastic and elastic interface. Furthermore, the transmission gradually gets smaller above the first band gap and all band gaps are widened. It is worth mentioning that the imaginary part of the P_2 wave is non-zero from the zero frequency, similar to the single-phase result [93]. Meanwhile, the frequency response becomes small at low frequencies. It may be due to an energy loss caused by the relative viscous flow of the pore fluid with respect to the porous solid skeleton [48].

Next, the viscosity ($\eta=10^{-7}$ Pa s) of the pore fluid is introduced into the E/P system. Calculated results are presented in Fig. 16(c,d). Real parts [Fig. 16(c)] of the wave number for both the P and SV waves deviate from high symmetric points of the first Brillouin zone. At the same time, flat bands disappear. At low frequencies, a complete band gap around $f_a=800$ m/s is produced and corresponding transmission [Fig. 16(d)] decreases particularly fast. The second complete band gap around $f_a=1300$ m/s is widened.

5.9.2. The P/F and F/P systems with the sealed-pore interface

Fig. 17 illustrates the effect of the pore fluid viscosity ($\eta=10^{-7}$ Pa s) on wave propagation in the P/F and F/P systems with the sealed-pore interface. For the P/F system in Fig. 17(a), the complex band structure is only slightly affected. The real and imaginary parts of the avoided crossing start to separate and the imaginary part for the P_2

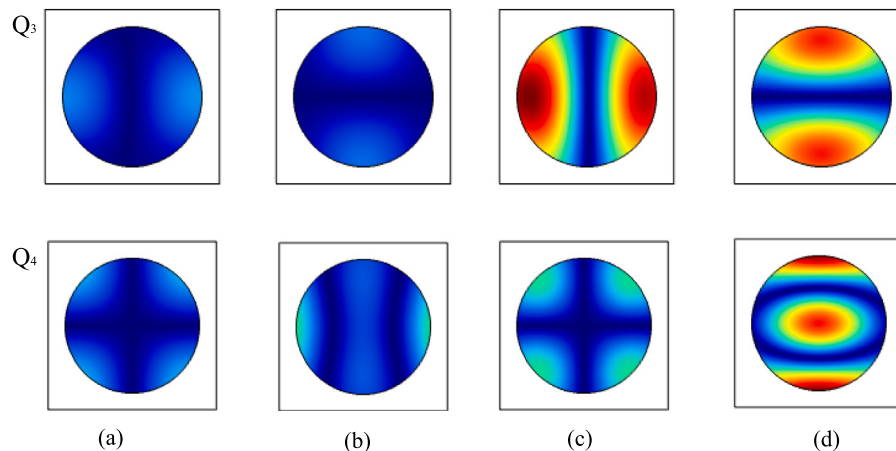


Fig. 10. Modal distributions at marked points Q_3 and Q_4 in Fig. 9(c,d). Panels (a), (b), (c), and (d) show normalized displacements $|u_x|/u_{\max}$, $|u_z|/u_{\max}$, $|U_x|/u_{\max}$, and $|U_z|/u_{\max}$, respectively. $u_{\max} = \max(|u_x|, |u_z|, |U_x|, |U_z|)$ at every marked point. The color scale is the same as in Fig. 3.

wave is slightly larger than for the P_1 wave. The first complete band gap moves up to the range 948m/s–990 m/s and the corresponding transmission is strengthened. The P_2 wave turns into an evanescent wave because the imaginary part of the P_2 wave is slightly larger at all frequencies. Transmission is reduced at low frequencies (below $f_a = 420$ m/s). However, the frequency response for the P_2 wave does not exhibit attenuation characteristics and is almost identical with the frequency response for the P_1 wave at high frequencies (above $f_a = 420$ m/s). The result from that the coupling between the P_1 and P_2 waves has a great influence on transmission at high frequencies. For the F/P system [Fig. 17(c)], it is easily found that the resonant band at low frequency and the corresponding transmission dip [Fig. 17(d)]. All in all, the viscosity has a little effect on the sealed-pore interface. It may be that the viscous pore fluid cannot flow across the interface and only can stay in the solid skeleton.

6. Conclusions

In this work, propagation of evanescent wave in hybrid metamaterials with interface effects has been analyzed based on the BOFEM technique. The finite element models of complex interfaces for elastic/poroelastic and fluid/poroelastic systems were built. The calculation method of complex band structures was developed, and the influence of interface conditions on wave propagation was discussed. The following observations and remarks can be made.

For the elastic/poroelastic interface, flat bands and locally resonant band gaps are found for both the P/E system (an elastic inclusion in a poroelastic matrix) and the E/P system (a poroelastic inclusion in an elastic matrix). However, the ‘quasi-resonance Bragg’ band gap is only formed for the P/E system. The ‘quasi-resonance Bragg’ band gap strongly depends on the radius and material parameters of the inclusion; it was not observed in previous studies of fluid-saturated porous media. In addition, a transition from an avoided-crossing to a wave-number band gap is observed by regulating geometric and material parameters of the elastic inclusion. For the E/P system, phase velocities of both the P and SV waves become smaller and resonant bands move down in frequency as the radius is increased. In addition, the stiffer the inclusion, the weaker the hybridization and the narrower the locally resonant band gap.

For the P/F system (a fluid inclusion in a poroelastic matrix), a cut-off frequency for the P_1 wave appears only for the open-pore interface. Attenuation is furthermore observed when two longitudinal waves band gaps overlap. Increasing the radius, the phase velocity of the SV wave becomes smaller than that of the P_2 wave. For the sealed-pore interface, a wide avoided crossing is produced. For the F/P system

(a poroelastic inclusion in a fluid matrix), the interface has little effect on the dispersion relation at low frequency.

When the viscosity is considered, band gaps and complex band structures are affected differently. For the P/E system, the transmission dip for the ‘quasi-resonance Bragg’ band gap disappears, but that for the local resonance band gap becomes slightly shallower and smoother than in the inviscid case. In addition, a complete band gap is found at low frequency for the E/P system. However, in contrast to the P/E system, the transmission dip of the first complete band gap becomes deeper than in the inviscid case for the P/F system. At the same time, flat bands disappear for the F/P system.

The present work only considers 2D hybrid single-phased and poroelastic systems but could naturally be extended to three-dimension(3D) cases. In this case, the complexity of wave equations would be increased because they would contain four independent variables. Moreover, the wave vector would have components in all three directions. Therefore, interface conditions would become more complex when establishing the finite element model. Besides, the present work is also relevant to the practical design of seismic metamaterials [94], and of importance for applications in natural soil and civil engineering [4], where the fluid phase and the viscosity of the soil are often ignored.

CRediT authorship contribution statement

Shu-Yan Zhang: Conceptualization, Validation, Methodology, software, Formal analysis, Visualization, Writing – original draft. **Jia-Chen Luo:** Methodology, Formal analysis. **Yan-Feng Wang:** Supervision, Writing – review & editing, Project administration. **Vincent Laude:** Discussion, Writing – review & editing. **Yue-Sheng Wang:** Supervision, Writing – review & editing, Project administration.

Declaration of competing interest

The authors declare that they have no known competing financial interests or personal relationships that could have appeared to influence the work reported in this paper.

Data availability

Data will be made available on request.

Acknowledgments

Financial support by the National Natural Science Foundation of China (12122207, 12021002, and 11991032) and the EIPHI Graduate School, China (ANR-17-EURE-0002) are gratefully acknowledged.

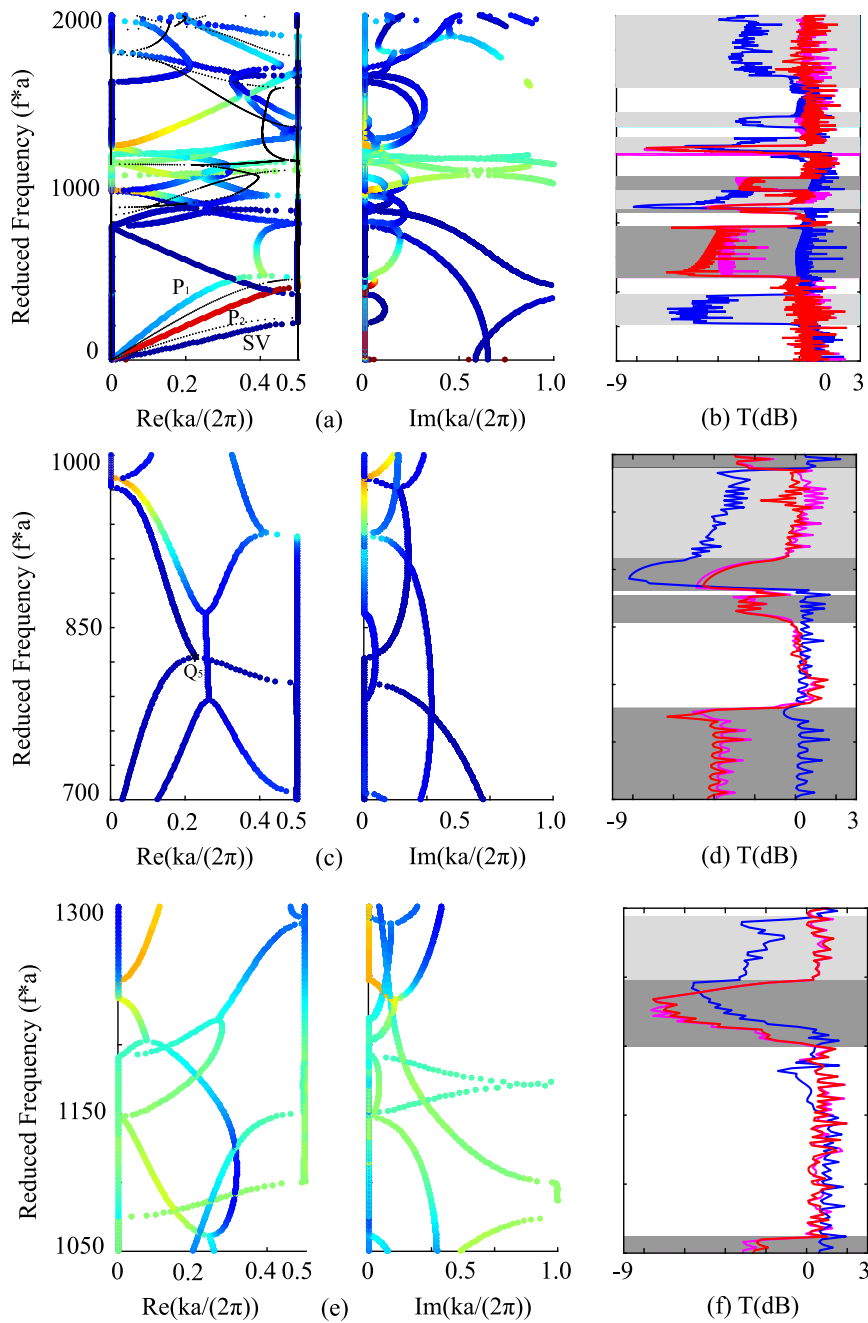


Fig. 11. Complex band structure and transmission spectrum for the P/F system (a fluid inclusion in a poroelastic matrix) with the sealed-pore interface. The left and right parts in panel (a) display the relation of the reduced frequency with the real and imaginary parts of the wave number. The color scale indicates wave polarization varying from blue (0) to red (1). Black dots are the real part of the P/F system with the open-pore interface. The calculated transmission spectrum is plotted in panel (b). The red, blue, and pink solid lines are for the responses to incident signals $(1,0,0)$, $(0,1,0)$, and $(0,0,1)$, respectively. Light gray regions represent band gaps for SV waves, whereas gray regions represent band gaps for two longitudinal waves. Panels (c-f) are zoomed complex band structures and transmission spectra in the reduced frequency regions $700 \text{ m/s}-1000 \text{ m/s}$ and $1050 \text{ m/s}-1300 \text{ m/s}$.

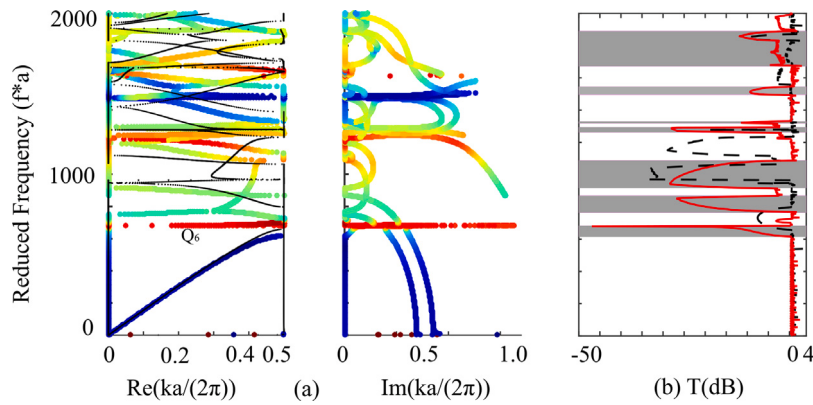


Fig. 12. The complex band structure and the transmission spectrum for the F/P system (a poroelastic inclusion in a fluid matrix) with the sealed-pore interface. The left and right parts in panel (a) display the relation of the reduced frequency with the real and imaginary parts of the wave number. The color scale indicates the ratio of the kinetic energy of the pore fluid to the total kinetic energy of the inclusion, from 0 (blue) to 1 (red). Black dots present the real part of the complex band structure for the F/P system with the open-pore interface. The calculated transmission spectrum is plotted in panel (b). The red solid line is for the received signal $\log_{10} |p|$ under a unit excitation. The black dashed line is for the transmission spectrum of the open-pore interface. Gray regions indicate band gaps for longitudinal waves.

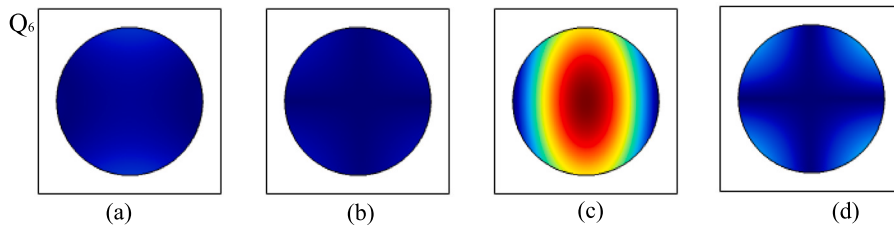


Fig. 13. Modal distribution at the marked point (Q_6) in Fig. 12(a). Panels (a), (b), (c), and (d) show normalized displacements $|u_x|/u_{\max}$, $|u_z|/u_{\max}$, $|U_x|/u_{\max}$, and $|U_z|/u_{\max}$, respectively. $u_{\max} = \max(|u_x|, |u_z|, |U_x|, |U_z|)$ at marked point. The color scale is the same as in Fig. 3.

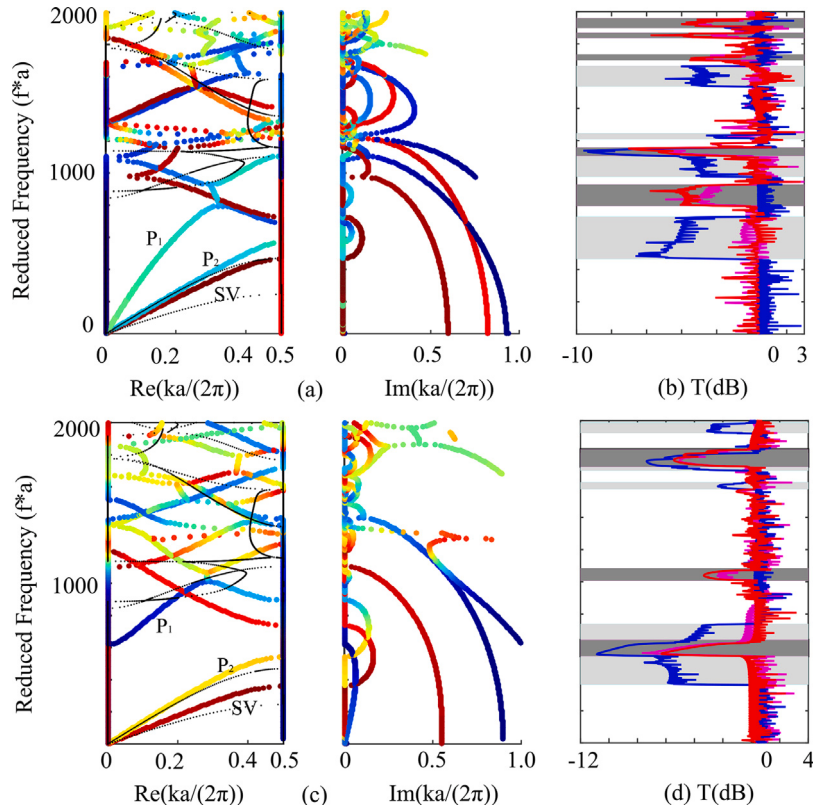


Fig. 14. Influence of the normalized radius r/a on the complex band structure and the frequency response for the P/F system (a fluid inclusion in a poroelastic matrix) with the open-pore interface. Panels (a,b) and panels (c,d) show results for $r/a=0.2$ and 0.3 , respectively. The color scale indicates the ratio of the kinetic energy of the pore fluid to the total kinetic energy in the matrix, from 0 (blue) to 1 (red). Black dots show the real part for $r/a=0.4$. The red, blue, and pink solid lines are for responses to excitation signals $(1,0,0)$, $(0,1,0)$, and $(0,0,1)$, respectively. Light gray regions represent band gaps for SV waves, whereas gray regions represent band gaps for two longitudinal waves.

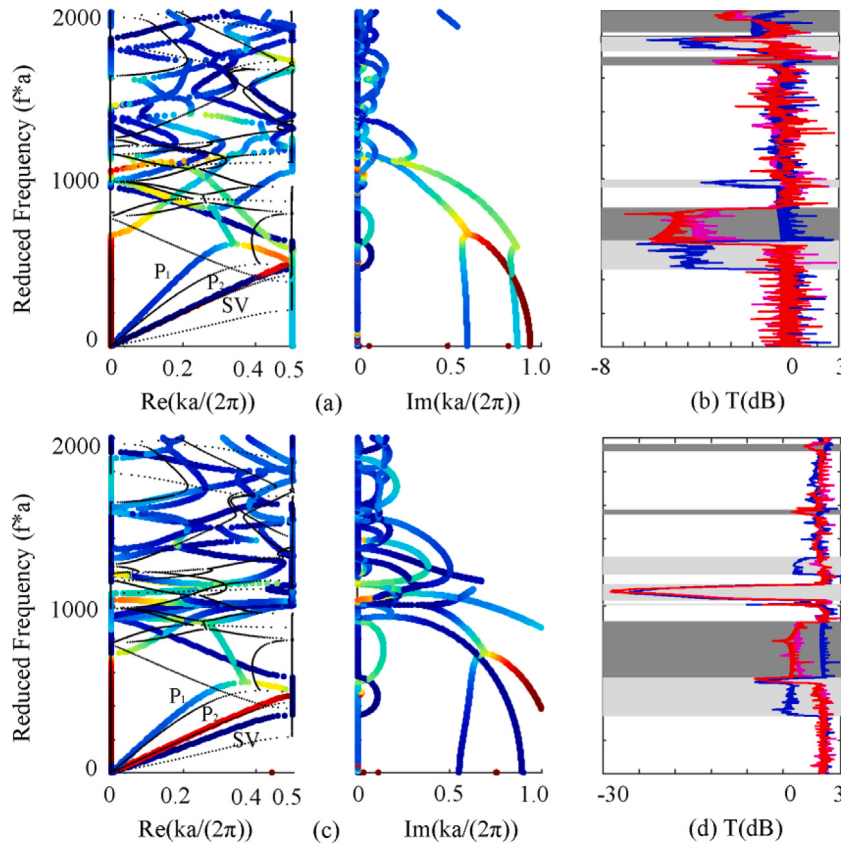


Fig. 15. Influence of the normalized radius r/a on the complex band structure and the frequency response for the P/F system (a fluid inclusion in a poroelastic matrix) with the sealed-pore interface. Panels (a,b) and panels (c,d) show results for $r/a=0.2$ and 0.3 , respectively. The color scale indicates the ratio of the kinetic energy of the pore fluid to the total kinetic energy in the matrix, from 0 (blue) to 1 (red). Black dots show the real part for $r/a=0.4$. The red, blue, and pink solid lines are for the responses to excitation signals $(1,0,0)$, $(0,1,0)$, and $(0,0,1)$, respectively. Light gray regions represent band gaps for SV waves, whereas gray regions represent band gaps for two longitudinal waves.

Appendix A. Basic equations of Biot's poroelastodynamics

The constitutive equations for transversely isotropic poroelastic medium can be expressed as [91]

$$\begin{bmatrix} \sigma_{xx} \\ \sigma_{yy} \\ \sigma_{zz} \\ \sigma_{xy} \\ \sigma_{yz} \\ \sigma_{zx} \\ p \end{bmatrix} = \begin{bmatrix} 2\mathbf{B}_1 + \mathbf{B}_2 & \mathbf{B}_2 & \mathbf{B}_3 & 0 & 0 & 0 & \mathbf{B}_6 \\ \mathbf{B}_2 & 2\mathbf{B}_1 + \mathbf{B}_2 & \mathbf{B}_3 & 0 & 0 & 0 & \mathbf{B}_6 \\ \mathbf{B}_3 & \mathbf{B}_3 & \mathbf{B}_4 & 0 & 0 & 0 & \mathbf{B}_7 \\ 0 & 0 & 0 & 2\mathbf{B}_1 & 0 & 0 & 0 \\ 0 & 0 & 0 & 0 & 2\mathbf{B}_5 & 0 & 0 \\ 0 & 0 & 0 & 0 & 0 & 2\mathbf{B}_5 & 0 \\ \mathbf{B}_6 & \mathbf{B}_6 & \mathbf{B}_7 & 0 & 0 & 0 & \mathbf{B}_8 \end{bmatrix} \begin{bmatrix} \epsilon_{xx} \\ \epsilon_{yy} \\ \epsilon_{zz} \\ \epsilon_{xy} \\ \epsilon_{yz} \\ \epsilon_{zx} \\ \xi \end{bmatrix}, \quad (\text{A.1})$$

where

$$\begin{aligned} \boldsymbol{\varepsilon} &= \frac{1}{2} (\nabla \mathbf{u} + (\nabla \mathbf{u})^T), \\ \xi &= -\nabla \cdot \mathbf{w}, \\ \mathbf{w} &= \varphi(\mathbf{U} - \mathbf{u}). \end{aligned} \quad (\text{A.2})$$

Here, σ_{ij} is the total stress related to both the solid skeleton strain (ϵ_{ij}) and to the increment of the fluid content per unit volume (ξ); $i, j=x, y, z$ represent the different spatial components; and p is the pore fluid pressure. \mathbf{w} denotes the relative displacement vector (with respect to the solid frame) of the pore fluid; φ is the porosity of the medium; \mathbf{u} and \mathbf{U} are the displacement vectors of the porous solid skeleton and the pore fluid, respectively. The material coefficients B_1 to B_8 are spatially

periodic functions determined by the porous solid skeleton and the pore fluid [95]:

$$\begin{aligned} B_1 &= C_{66}, \\ B_2 &= C_{12} + B_6^2/B_8, \\ B_3 &= C_{13} + B_6 B_7/B_8, \\ B_4 &= C_{33} + B_7^2/B_8, \\ B_5 &= C_{44}, \\ B_6 &= -\left(1 - \frac{C_{11} + C_{12} + C_{13}}{3K_S}\right) B_8, \\ B_7 &= -\left(1 - \frac{(2C_{13} + C_{33})}{3K_S}\right) B_8, \\ B_8 &= \left(\frac{1-\varphi}{K_S} + \frac{\varphi}{K_f} - \frac{2C_{11} + 2C_{12} + 4C_{13} + C_{33}}{9K_S^2}\right)^{-1}, \end{aligned} \quad (\text{A.3})$$

where C_{ij} are the elastic constants of the porous solid skeleton; and K_S and K_f are the bulk modulus of the porous solid skeleton and pore fluid, respectively.

For an isotropic poroelastic medium, we have

$$B_4 = 2B_1 + B_2, \quad B_3 = B_2, \quad B_5 = B_1, \quad B_7 = B_6. \quad (\text{A.4})$$

Substituting Eq. (A.4) into (A.1), the constitutive equations can be simplified as

$$\begin{aligned} \boldsymbol{\sigma} &= B_2 \nabla \cdot \mathbf{u} \cdot \mathbf{I} + 2B_5 \boldsymbol{\varepsilon} - B_6 \nabla \cdot \mathbf{w} \cdot \mathbf{I}, \\ p &= B_6 \nabla \cdot \mathbf{u} - B_8 \nabla \cdot \mathbf{w}. \end{aligned} \quad (\text{A.5})$$

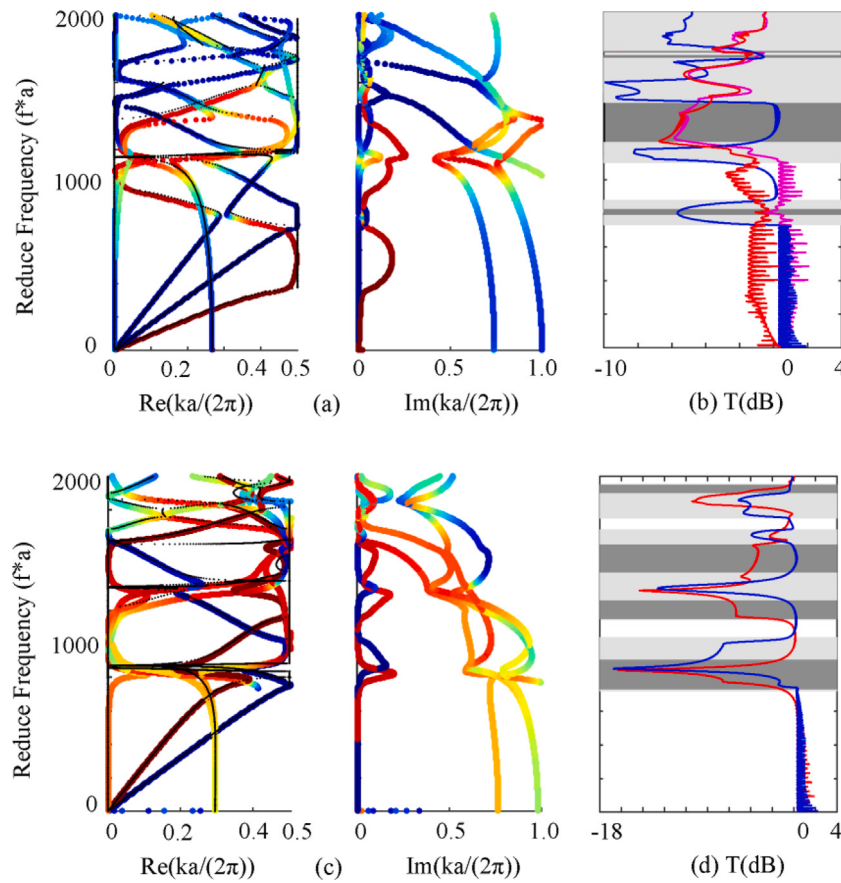


Fig. 16. Influence of the pore fluid viscosity on the complex band structure and the transmission spectrum for the poroelastic/elastic interface. Panels (a) and (c) present the variation of the real and imaginary wave numbers with the reduced frequency for the P/E and E/P systems, respectively. Black dots present the real part of the complex band structure for an inviscid pore fluid. Color scales are the same as in Fig. 2(a) and Fig. 4(a), respectively. Panels (b) and (d) represent the frequency response functions for the P/E and E/P systems, respectively. Line types, the light gray and gray regions are similar to the inviscid fluid case.

Based on Biot's theory, the equations of motion for wave propagation in an isotropic poroelastic medium can be written in Cartesian coordinates as

$$\nabla \cdot \sigma = -\omega^2 (\rho \mathbf{u} + \rho_f \mathbf{w}), \\ \nabla p = \omega^2 \rho_f \mathbf{u} + \omega^2 \bar{\mathbf{m}} \cdot \omega. \quad (\text{A.6})$$

where $\rho = (1 - \varphi) \rho_s + \varphi \rho_f$ represents the density of the poroelastic medium; ρ_s and ρ_f are the mass densities of porous solid skeleton and pore fluid, respectively; and ω is angular frequency. $\bar{\mathbf{m}} = \text{diag}[\bar{m}_1, \bar{m}_2, \bar{m}_3]$, $\bar{m}_1 = m_{11} + ir_{11}/\omega$, $\bar{m}_2 = m_{22} + ir_{22}/\omega$, and $\bar{m}_3 = m_{33} + ir_{33}/\omega$. m_{ii} and r_{ii} are coefficients introduced by Biot. For isotropic poroelastic medium, we have $m_{11} = m_{22} = m_1$, $m_{33} = m_3$, $r_{11} = r_{22} = r_1$, and $r_{33} = r_3$. They are all functions of angular frequency ω and can be stated as

$$m_i = \text{Re} [\alpha_i(\omega)] \rho_f / \varphi, \\ r_i = \text{Re} [\eta / K_i(\omega)]. \quad (\text{A.7})$$

Here, η is the viscosity of the pore fluid; and $\alpha_i(\omega)$ and $K_i(\omega)$ are the dynamic tortuosity and permeability, respectively. The relationship between $\alpha_i(\omega)$ and $K_i(\omega)$ can be expressed as

$$\alpha_i(\omega) = i\eta\varphi / [\omega\rho_f K_i(\omega)], \quad (\text{A.8})$$

For a poroelastic medium with simple pore, the dynamic permeability $K_i(\omega)$ can be approximately defined as

$$K_i(\omega) = K_i(0) \left(\left[1 - \frac{4i\alpha_i(\infty) K_i(0) \omega \rho_f}{\eta d_i^2 \varphi^2} \right]^{1/2} - \frac{i\alpha_i(\infty) K_i(0) \omega \rho_f}{\eta \varphi} \right)^{-1}, \quad (\text{A.9})$$

where d_i^2 is the pore characteristic size and $K_i(0)$ can be measured independently. When the pores are not connected, we further have $8\alpha_i(\infty) K_i(0) / \varphi d_i^2 = 1$.

Appendix B. Numerical validation

In this appendix, the calculation method for the complex band structure of the P/E and F/P systems is validated. We assume the elastic inclusion to be the poroelastic one with a tiny porosity. Then the wave behaviors in the P/P (F/P) system would be similar to those in P/E (F/E) system. The related results are shown in Fig. B.18. For panel (a), blue stars represent the complex band structure for the P/P system described in Ref. [50] with $\phi_2 = 1e^{-8}$ for the inclusion. Red dots are the corresponding results for the P/E system. It can be found that the real and imaginary parts of the wave number almost coincide with each other. Blue stars and red dots in panel (b) are the complex band structures for the F/E and F/P systems, respectively. A good agreement is also observed. So the proposed method for the calculation of complex band structure of poroelastic–elastic (or fluid) system is valid.

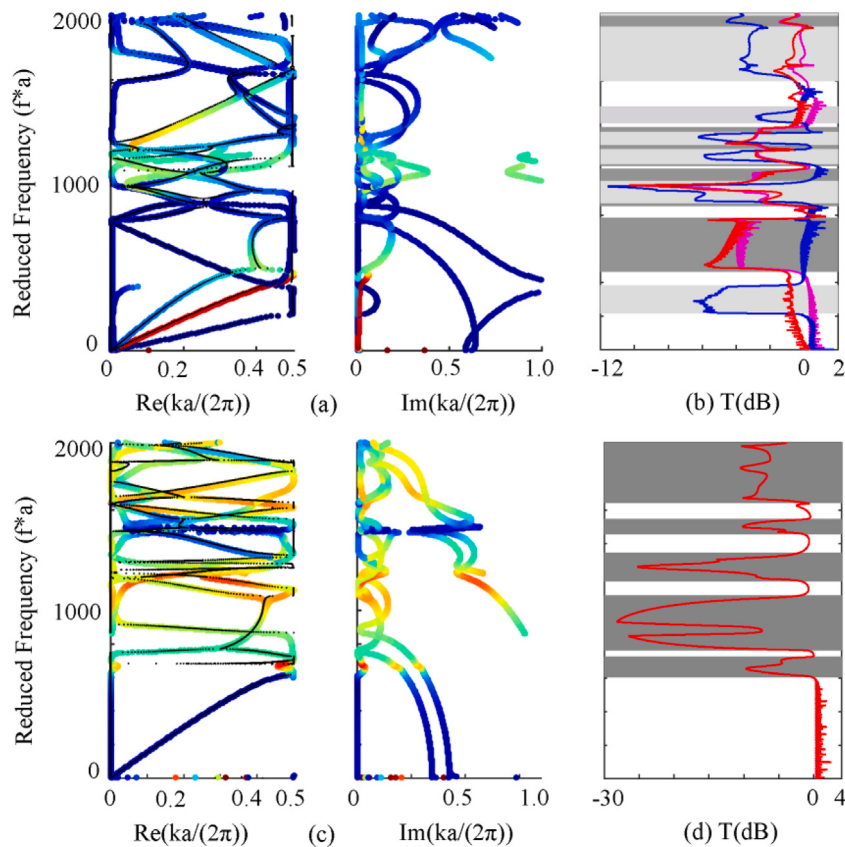


Fig. 17. Influence of the pore fluid viscosity on the complex band structure and the transmission spectrum for 2D fluid and poroelastic metamaterials with the sealed-pore interface. Panels (a) and (c) present the variation of the real and imaginary wave numbers with the reduced frequency for the P/F and F/P systems, respectively. Black dots present the real part of the complex band structure for an inviscid pore fluid. Panels (b) and (d) represent the frequency response functions for the P/F and F/P systems, respectively. The line types, and the light and gray regions are similar to the inviscid fluid case.

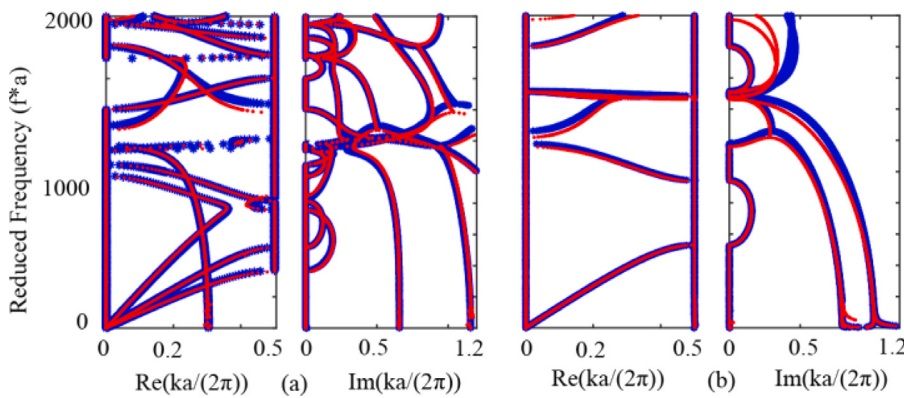


Fig. B.18. Blue stars and red dots of panel (a) are the complex band structures for the P/P and the P/E systems; respectively. Blue stars and red dots of panel (b) are the complex band structures for the P/P and fluid/solid systems; respectively.

References

- [1] Kushwaha MS, Halevi P, Dobrzynski L, Djafari-Rouhani B. Acoustic band structure of periodic elastic composites. *Phys Rev Lett* 1993;71:2022–5.
- [2] Sugino C, Leadenham S, Ruzzene M, Erturk A. On the mechanism of bandgap formation in locally resonant finite elastic metamaterials. *J Appl Phys* 2016;120:134501.
- [3] Thota M, Wang K. Reconfigurable origami sonic barriers with tunable bandgaps for traffic noise mitigation. *J Appl Phys* 2017;122:154901.
- [4] Brule S, Javelaud E, Enoch S, Guenneau S. Experiments on seismic metamaterials: molding surface waves. *Phys Rev Lett* 2014;112:133901.
- [5] Liu ZY, Zhang XX, Mao YW, Zhu YY, Yang ZY, Chan CT, et al. Locally resonant sonic materials. *Science* 2000;338:201–5.
- [6] Vasseur JO, Deymier PA, Chenni B, Djafari RB, Dobrzynski L, Prevost D. Experimental and theoretical evidence for the existence of absolute acoustic band gaps in two-dimensional solid phononic crystals. *Phys Rev Lett* 2001;86:3012.
- [7] Zhou XZ, Wang YS, Zhang CZ. Three-dimensional sonic band gaps tunned by material parameters. *Appl Mech Mater* 2010;29–32:1797–802.
- [8] Tamaka Y, Tomoyasu Y, Tamura SI. Band structure of acoustic waves in phononic lattices: Two-dimensional composites with large acoustic mismatch. *Phys Rev B* 2000;62:7387–92.
- [9] Sun J, Wei P. Band gaps of 2D phononic crystal with imperfect interface. *Mech Adv Mater Struct* 2014;21:107–16.
- [10] Hamilton EL. Reflection coefficients and bottom losses at normal incidence computed from Pacific sediment properties. *Geophysics* 1970;35:995–1004.
- [11] Zhang JS, Jeng DS, Liu LF, Zhang C, Zhang Y. Response of a porous seabed to water waves over permeable submerged breakwaters with Bragg reflection. *Ocean Eng* 2012;43:1–12.

- [12] Cruz DLV, Spanos TJT. Seismic wave propagation in a porous medium. *Geophysics* 1985;50:1556–65.
- [13] Madeo A, Gavriluk S. Propagation of acoustic waves in porous media and their reflection and transmission at a pure-fluid/porous-medium permeable interface. *Eur J Mech A Solids* 2010;29:897–910.
- [14] Biot MA. Theory of propagation of elastic waves in a fluid-saturated porous solid: II. Higher frequency range. *J Acoust Soc Am* 1956;28:168–78.
- [15] Deresiewicz H, Skalak R. On uniqueness in dynamic poroelasticity. *Bull Seismol Soc Amer* 1963;53:783–8.
- [16] Vashisth AK, Sharma MD, Gogna ML. Reflection and transmission of elastic waves at a loosely bonded interface between an elastic solid and liquid-saturated porous solid. *Geophys J R Astron Soc* 1991;105:601–17.
- [17] Feng S, Shechao D. High-frequency acoustic properties of a fluid/porous solid interface. I. New surface mode. *J Acoust Soc Am* 1983;74:906–14.
- [18] Rosenbaum J. Synthetic microseismograms: logging in porous formation. *Geophysics* 1974;39:1–14–32.
- [19] Markov MG. Reflection of elastic waves at an interfaces between two porous half-spaces filled with different fluids. *Phys Solid Earth* 2009;45:769–76.
- [20] Kumar M, Sharma MD. Reflection and transmission of attenuated waves at the boundary between two dissimilar poroelastic solids saturated with two immiscible viscous fluids. *Geophys Prospect* 2013;61:1035–55.
- [21] Lyu DD, Wang JT, Jin F, Zhang CH. Reflection and transmission of plane waves at a water-porous sediment interface with a double-porosity substrate. *Transp Porous Media* 2014;103:25–45.
- [22] Rasolofosaon PNJ. Importance of interface hydraulic condition on the generation of second bulk compressional wave in porous media. *Appl Phys Lett* 1988;52:780–2.
- [23] Smeulders DM. Experimental evidence for slow compressional waves. *J Eng Mech* 2005;131:908–17.
- [24] Dai ZJ, Kuang ZB, Zhao SX. Reflection and transmission of elastic waves from the interface of a fluid-saturated porous solid and a double porosity solid. *Transp Porous Media* 2006;65:237–64.
- [25] Sharma MD, Saini T. Pore alignment between two dissimilar saturated poroelastic media: Reflection and refraction at the interface. *Int J Solids Struct* 1992;29:1361–77.
- [26] Sharma MD. Wave propagation across the boundary between two dissimilar poroelastic solids. *J Sound Vib* 2008;314:657–71.
- [27] Vashisth AK, Khurana P. Waves in stratified anisotropic poroelastic media: a transfer matrix approach. *J Sound Vib* 2004;277:239–75.
- [28] Hajra S, Mukhopadhyay A. Reflection and refraction of seismic waves incident obliquely at the boundary of a liquid-saturated porous solid. *Bull Seismol Soc Am* 1982;72:1509–33.
- [29] Dai ZJ, Kuang ZB, Zhao SX. Reflection and transmission of elastic waves at the interface between an elastic solid and a double porosity medium. *Int J Rock Mech Min Sci* 2006;43:961–71.
- [30] Wang JT, Jin F, Zhang CH. Reflection and transmission of plane waves at an interface of water/porous sediment with underlying solid substrate. *Ocean Eng* 2013;63:8–16.
- [31] Sharma MD, Kaushik VP, Gogna ML. Reflection and refraction of plane waves at an interface between liquid-saturated porous solid and viscoelastic solid. *Quart J Mech Appl Math* 1990;43:427–48.
- [32] Sharma MD, Gogna ML. Reflection and refraction of plane harmonic waves at an interface between elastic solid and porous solid saturated by viscous liquid. *Pure Appl Geophys* 1992;138:249–66.
- [33] Peng H, Sripanich Y, Vasconcelos I, Trampert J. Benchmarking wave equation solvers using interface conditions: the case of porous media. *Geophys J Int* 2021;224:355–76.
- [34] Goyal S, Tomar SK. Reflection/refraction of a dilatational wave at a plane interface between uniform elastic and swelling porous half-spaces. *Transp Porous Media* 2015;109:609–32.
- [35] Yang J. Importance of flow condition on seismic waves at a saturated porous solid boundary. *J Sound Vib* 1999;221:391–413.
- [36] Barak MS, Kumari M, Kumar M. Effect of local fluid flow on the propagation of plane waves at an interface of water/double-porosity solid with underlying uniform elastic solid. *Ocean Eng* 2018;147:195–205.
- [37] Vashisth AK, Sharma MD, Gogna ML. Reflection and transmission of elastic waves at a loosely bonded interface between an elastic solid and liquid-saturated porous solid. *Geophys J Int* 1991;105:601–17.
- [38] Singh B, Singh S. Reflection and transmission of elastic waves at a loosely bonded interface between an elastic solid and a viscoelastic porous solid saturated by viscous liquid. *Glob J Res Eng* 2014;14:1–13.
- [39] Denneman A, Drijkoningen G, Smeulders D, Wapenaar C. Reflection and transmission of waves at a fluid/porous-medium boundary. In: IUTAM symposium on theoretical and numerical methods in continuum mechanics of porous materials. Springer; 2001, p. 343–50.
- [40] Bouzidi Y, Schmitt DR. Incidence-angle-dependent acoustic reflections from liquid-saturated porous solids. *Geophys J Int* 2012;191:1427–40.
- [41] Denneman A, Drijkoningen G, Smeulders D, Wapenaar K. Reflection and transmission of waves at a fluid/porous-medium interface. *Geophysics* 2002;67:282–91.
- [42] Dai ZJ, Kuang ZB. Reflection and transmission of elastic waves at the interface between water and a double porosity solid. *Transp Porous Media* 2008;72:369–92.
- [43] Wu KY, Xue Q, Laszlo A. Reflection and transmission of elastic waves from a fluid-saturated porous solid boundary. *J Acoust Soc Am* 1990;87:2349–58.
- [44] Chiavassa G, Lombard B. Wave propagation across acoustic/Biot's media: a finite-difference method. *Commun Comput Phys* 2013;13:985–1012.
- [45] Lefeuve MG, Mesgouez A, Chiavassa G, Lombard B. Semi-analytical and numerical methods for computing transient waves in 2D acoustic/poroelastic stratified media. *Wave Motion* 2012;49:667–80.
- [46] Magliacano D, Ouisse M, Khelif A, De Rosa S, Franco F, Atalla N, et al. Computation of dispersion diagrams for periodic porous materials modeled as equivalent fluids. *Mech Syst Signal Process* 2020;142:106749.
- [47] Xiong L, Nennig B, Aurégan Y, Bi WP. Sound attenuation optimization using metamorphic materials tuned on exceptional points. *J Acoust Soc Am* 2017;142:2288–97.
- [48] Lewińska MA, Dommelen J, Kouznetsova VG, Geers M. Towards acoustic metafoams: the enhanced performance of a poroelastic material with local resonators. *J Mech Phys Solids* 2019;124:189–205.
- [49] Wang YF, Liang JW, Chen AL, Wang YS, Laude V. Wave propagation in one-dimensional fluid-saturated porous metamaterials. *Phys Rev B* 2019;99:134304.
- [50] Wang YF, Liang JW, Chen AL, Wang YS, Laude V. Evanescent waves in two-dimensional fluid-saturated porous metamaterials with a transversely isotropic matrix. *Phys Rev B* 2020;101:184301.
- [51] Zhang SY, Yan DJ, Wang YS, Wang YF, Laude V. Wave propagation in one-dimensional fluid-saturated porous phononic crystals with partial-open pore interfaces. *Int J Mech Sci* 2021;195:106227.
- [52] Fama A, Restuccia L, Jou D. A simple model of porous media with elastic deformations and erosion or deposition. *Z Angew Math Phys* 2020;71:1–21.
- [53] Rohan E, Cimrman R. Modelling wave dispersion in fluid saturating periodic scaffolds. *Appl Math Comput* 2021;401:126256.
- [54] Pu XB, Palermo A, Cheng ZB, Shi ZF, Marzani A. Seismic metasurfaces on porous layered media: Surface resonators and fluid-solid interaction effects on the propagation of Rayleigh waves. *Internat J Engrg Sci* 2020;154:103347.
- [55] Laude V, Achaoui Y, Benchabane S, Khelif A. Evanescent Bloch waves and the complex band structure of phononic crystals. *Phys Rev B* 2009;80:092301.
- [56] Miranda E, Santos J. Evanescent Bloch waves and complex band structure in magnetoelectroelastic phononic crystals. *Mech Syst Signal Process* 2018;112:280–304.
- [57] Hui Z, Zhang C, Wang Y, Sladek J, Sladek V. A meshfree local RBF collocation method for anti-plane transverse elastic wave propagation analysis in 2D phononic crystals. *J Comput Phys* 2016;305:997–1014.
- [58] Ao X, Chan CT. Complex band structures and effective medium descriptions of periodic acoustic composite systems. *Phys Rev B* 2009;80:308–10.
- [59] Li FL, Zhang C, Wang YS. Analysis of the effects of viscosity on the SH-wave band-gaps of 2D viscoelastic phononic crystals by Dirichlet-to-Neumann map method. *Int J Mech Sci* 2021;195:106225.
- [60] Wang Y-F, Zhang S-Y, Wang Y-S, Laude V. Hybridization of resonant modes and Bloch waves in acoustoelastic phononic crystals. *Phys Rev B* 2020;102:144303.
- [61] Veres IA, Berer T. Complexity of band structures: Semi-analytical finite element analysis of one-dimensional surface phononic crystals. *Phys Rev B Condens Matter* 2012;86:64–73.
- [62] Antonio P, Alessandro M. Extended bloch mode synthesis: Ultrafast method for the computation of complex band structures in phononic media. *Int J Solids Struct* 2016;100:101–29–40.
- [63] Palermo A, Marzani A. A reduced Bloch operator finite element method for fast calculation of elastic complex band structures. *Int J Solids Struct* 2020;191–192:601–13.
- [64] Atalla N, Panneton R, Debergue P. A mixed displacement-pressure formulation for poroelastic materials. *J Acoust Soc Am* 1998;104:1444–52.
- [65] Atalla N, Hamdi MA, Panneton R. Enhanced weak integral formulation for the mixed (u, p) poroelastic equations. *J Acoust Soc Am* 2001;109:3065–8.
- [66] Debergue P, Panneton R, Atalla N. Boundary conditions for the weak formulation of the mixed (u, p) poroelasticity problem. *J Acoust Soc Am* 1999;106:2383–90.
- [67] Dell'Isola F, Madeo A, Seppecher P. Boundary conditions at fluid-permeable interfaces in porous media: A variational approach. *Int J Solids Struct* 2009;46:3150–64.
- [68] Batifol C, Zielinski TG, Ichchou MN, Galland MA. A finite-element study of a piezoelectric/poroelastic sound package concept. *Smart Mater Struct* 2007;16:168–77.
- [69] Zielinski TG. Multiphysics modeling and experimental validation of the active reduction of structure-borne noise. *J Vib Acoust* 2010;132:061008.
- [70] Bernier NR, Tóth LD, Feofanov AK, Kippenberg TJ. Level attraction in a microwave optomechanical circuit. *Phys Rev A* 2018;98:023841.
- [71] Castel V, Jeunehomme R, Youssef JB, Vukadinovic N, Manchec A, Dejene FK, et al. Thermal control of the magnon-photon coupling in a notch filter coupled to a yttrium iron garnet/platinum system. *Phys Rev B* 2017;96:064407.
- [72] Krushynska AO, Kouznetsova VG, Geers MG. Visco-elastic effects on wave dispersion in three-phase acoustic metamaterials. *J Mech Phys Solids* 2016;96:29–47.

- [73] Bhoi B, Kim B, Jang SH, Kim J, Yang J, Cho YJ, et al. Abnormal anticrossing effect in photon-magnon coupling. *Phys Rev B* 2019;99:134426.
- [74] Sainidou R, Stefanou N, Modinos A. Formation of absolute frequency gaps in three-dimensional solid phononic crystals. *Phys Rev B* 2002;66:212301.
- [75] Ao XY, Chan CT. Complex band structures and effective medium descriptions of periodic acoustic composite systems. *Phys Rev B* 2009;80:235118.
- [76] Krushynska AO, Minciari M, Bosia F, Pugno NM. Coupling local resonance with Bragg band gaps in single-phase mechanical metamaterials. *Extreme Mech Lett* 2017;12:30–6.
- [77] Davis BL, Hussein MI. Nanophononic metamaterial: Thermal conductivity reduction by local resonance. *Phys Rev Lett* 2014;112:055505.
- [78] Zhao L, Lu ZQ, Ding H, Chen LQ. Experimental observation of transverse and longitudinal wave propagation in a metamaterial periodically arrayed with nonlinear resonators. *Mech Syst Signal Process* 2022;108836:170.
- [79] Goffaux C, Sánchez-Dehesa J, Yeyati AL, Lambin P, Khelif A, Vasseur JO, et al. Evidence of Fano-like interference phenomena in locally resonant materials. *Phys Rev Lett* 2002;88:225502.
- [80] Yu CH, Yang Y, Rao JW, Hyde P, Wang YP, Zhang B, et al. Spin number dependent dissipative coupling strength. *AIP Adv* 2019;9:115012.
- [81] Zhang HF, Liu SB, Kong XK. Dispersion properties of three-dimensional plasma photonic crystals in diamond lattice arrangement. *J Lightwave Technol* 2013;31:1694–702.
- [82] Vasseur JO, Deymier PA, Frantziskonis G, Hong G, Djafari-Rouhani B, Dobrzynski L. Experimental evidence for the existence of absolute acoustic band gaps in two-dimensional periodic composite media. *J Phys Condens Matter* 1998;10:6051.
- [83] Mace BR, Manconi E. Wave motion and dispersion phenomena: Veering, locking and strong coupling effects. *J Acoust Soc Am* 2012;131:1015–28.
- [84] Sievenpiper DF, Sickmiller ME, Yablonovitch E. 3D wire mesh photonic crystals. *Phys Rev Lett* 1996;76:2480.
- [85] Chen YY, Qian F, Scarpa F, Zuo L, Zhuang XY. Harnessing multi-layered soil to design seismic metamaterials with ultralow frequency band gaps. *Mater Des* 2019;175:107813.
- [86] Eric L, He ZC, Wang G, Yong J. Fundamental study of mechanism of band gap in fluid and solid/fluid phononic crystals. *Adv Eng Softw* 2018;121:167–77.
- [87] Soliman YM, Su MF, Leseman ZC, Reinke CM, Olsson RH. Effect of release holes on micro-scale solid-solid phononic crystals. *Appl Phys Lett* 2010;97:081907.
- [88] Pokrovsky AL, Kamaev V, Li CY, Vardeny ZV, Efros AL, Kurdyukov DA, et al. Theoretical and experimental studies of metal-infiltrated opals. *Phys Rev B* 2005;71:165114.
- [89] Luo M, Liu QH. Three-dimensional dispersive metallic photonic crystals with a bandgap and a high cutoff frequency. *J Opt Soc Amer A* 2010;27:1878–84.
- [90] Wijesinghe AM, Kingsbury HB. On the dynamic behavior of poroelastic materials. *J Acoust Soc Am* 1979;65:90–5.
- [91] Biot MA. Mechanics of deformation and acoustic propagation in porous media. *J Appl Phys* 1962;33:1482–98.
- [92] Wang YF, Wang YS, Laude V. Wave propagation in two-dimensional viscoelastic metamaterials. *Phys Rev B* 2015;92:104110.
- [93] Lou J, He L, Yang J, Kitipornchai S, Wu H. Wave propagation in viscoelastic phononic crystal rods with internal resonators. *Appl Acoust* 2018;141:382–92.
- [94] Zeng Y, Xu Y, Deng K, Zeng ZX, Yang HW, Muzamil M, et al. Low-frequency broadband seismic metamaterial using I-shaped pillars in a half-space. *J Appl Phys* 2018;123:214901.
- [95] Kazi-Aoual MN, Bonnet G, Jouanna P. Green's functions in an infinite transversely isotropic saturated poroelastic medium. *J Acoust Soc Am* 1988;84:1883–9.